

BLR Physical Conditions in Extreme Population A Quasars: a Method to Estimate Central Black Hole Mass at High Redshift

C. Alenka Negrete and Deborah Dultzin

Instituto de Astronomía, Universidad Nacional Autónoma de México, Mexico

anegrete@astro.unam.mx, deborah@astro.unam.mx

Paola Marziani

INAF, Astronomical Observatory of Padova, Italy

paola.marziani@oapd.inaf.it

and

Jack W. Sulentic

Instituto de Astrofísica de Andalucía, Spain

sulentic@iaa.es

ABSTRACT

We describe a method for estimating physical conditions in the broad line region (BLR) for a significant subsample of Seyfert-1 nuclei and quasars. Several diagnostic ratios based on intermediate (AlIII λ 1860, SiIII] λ 1892) and high (CIV λ 1549, SiIV λ 1397) ionization lines in the UV spectra of quasars are used to constrain density, ionization and metallicity of the emitting gas. We apply the method to two extreme Population A quasars – the prototypical NLSy1 I Zw 1 and higher z source SDSS J120144.36+011611.6. Under assumptions of spherical symmetry and pure photoionization we infer BLR physical conditions: low ionization (ionization parameter $< 10^{-2}$), high density ($10^{12} - 10^{13} \text{ cm}^{-3}$) and significant metal enrichment. Ionization parameter and density can be derived independently for each source with an uncertainty that is less than ± 0.3 dex. We use the product of density and ionization parameter to estimate the BLR radius and derive an estimation of the virial black hole mass (M_{BH}). Estimates of M_{BH} based on the “photoionization” analysis described in this paper are probably more accurate than those derived from the mass – luminosity correlations widely employed to compute black hole masses for high redshift quasars.

Subject headings: quasars: general — quasars: individual (I Zw 1, SDSS J120144.36+011611.6)

1. Introduction

We lack a simple diagnostic method to estimate physical conditions (density, ionization parameter, metallicity) in the broad line region (BLR) of quasars. Techniques for estimating electron density and ionization in nebular astrophysics (Osterbrock & Ferland 2006) are not straightforwardly applicable to broad lines in quasars. Reasons include: large line widths, line doublets too closely spaced to resolve individual components, and density at least an order of magnitude higher than the critical density assumed for forbidden transitions modeled in spectra of planetary nebulae and HII regions. The ionization parameter U , that represents the dimensionless ratio of the number of ionizing photons and the electron density n_e or, equivalently, the total number density of hydrogen n_H ionized and neutral¹, can be estimated from the intensity ratio of two strong resonance lines arising from different ionic stages of the same element (Davidson & Netzer 1979). It is again not easy to interpret the results in the case of quasars. For example, the ratio CIII] λ 1909/CIV λ 1549 may not yield a meaningful value if the relatively low CIII] λ 1909 critical density implies that the line is formed at larger radii than CIV λ 1549. Using lines of different ions widens the choice of diagnostic line ratios although additional sources of uncertainty are introduced.

The presence of the strong CIII] λ 1909 emission line implies that electron density n_e cannot be very high. However, high density ($n_e \sim 10^{11-13} \text{cm}^{-3}$) is invoked to explain the rich low ionization spectrum (especially FeII) observed in quasars (e.g., Baldwin et al. 2004). Several lines in the UV spectrum of I Zw 1 (prominent FeII, relatively strong AlIII λ 1860, and CIII] λ 1176) point towards high density at least for the low ionization line (LIL) emitting zone (Baldwin et al. 1996; Laor et al. 1997b). This low ionization BLR (LIL BLR) has very similar properties to the OI and CaII emitting region identified by Matsuoka et al. (2008). The region where these LILs are produced cannot emit much CIII] λ 1909 if electron density exceeds 10^{11}cm^{-3} . But is the CIII] λ 1909 line really so strong in most quasars? BLR conditions are certainly complex and the assumption of a single emitting region cannot explain both LILs and high ionization lines (HILs) (Marziani et al. 2010; Wang et al. 2011, and references therein).

In this paper we report an analysis based on several diagnostic ratios used to constrain density, ionization parameter and metallicity in the BLR of two sources that are representative of the Narrow Line Seyfert 1 (NLSy1) sub-sample of quasars (§2). We use methodological considerations that enable us to deblend and identify the principal lines of the spectra (§3.1). Our sources show weak CIII] λ 1909 emission (relative to SiIII] λ 1892) simplifying interpreta-

¹ In a fully ionized medium $n_e \approx 1.2 n_H$. We prefer to adopt a definition based on n_H because it is the one employed in CLOUDY computations.

tion of the emission line spectrum (§3.2). Diagnostic ratios are heuristically defined (§4.1) and interpreted through an array of photo-ionization simulations (§4.2). We show that they converge toward well-defined values of ionization and density (§5). We also consider the influence of heating sources other than photoionization (§6.1). Under the assumption of a pure photoionized gas, the present analysis can be used to determine the product of density and ionization parameter enabling us to estimate the distance of the BLR from the central continuum source (r_{BLR}) and the virial black hole mass (M_{BH}) (§6.2). Finally, in §7 we give our conclusions.

1.1. The Eigenvector 1 Parameter Space

Boroson & Green (1992) (BG92) identified a series of correlations from principal component analysis (PCA) of the correlation matrix of emission line measures for a bright low-redshift quasar sample. The sample contained 87 PG quasars with $z \sim 0.5$ (17 of them radio-loud, RL). The first PCA eigenvector (hereafter E1) identified correlations involving broad $\text{H}\beta$, broad FeII and narrow $[\text{OIII}]\lambda\lambda 4959, 5007$ emission lines. In an effort to clarify the meaning of the E1, Sulentic et al. (2000) searched for a correlation diagram that showed maximal discrimination between the various Active Galaxy Nuclei (AGN) subclasses. The best E1 correlation space that we could identify involved measures of: 1) equivalent width of the FeII $\lambda 4570$ blend (defined as the ratio $R_{\text{FeII}} = W(\text{FeII}\lambda 4570)/W(\text{H}\beta)$) and 2) $\text{FWHM}(\text{H}\beta)$. These were supplemented with: 3) the soft X-ray photon index, Γ_{soft} and the centroid line shift of high ionization C IV $\lambda 1549$. Figure 7 of Sulentic et al. (2000) shows two-dimensional (2D) projections of this four-dimensional E1 (4DE1) space: $\text{FWHM}(\text{H}\beta)$ vs. R_{FeII} , Γ_{soft} vs. R_{FeII} and $\text{FWHM}(\text{H}\beta)$ vs. Γ_{soft} . They supplemented the BG92 RL sample with an additional 18 sources (with comparable signal-to-noise S/N spectra) taken from Marziani et al. (1996) who reported $W(\text{FeII})$ measures over the range 4240 – 5850 Å. The range 4240 – 5850 Å FeII flux was divided by a factor ≈ 3.3 in order to obtain the flux in the range 4434-4684 Å that was used by BG92 (both works relied on the same FeII template based on I Zw 1). Sulentic et al. (2000) separated the various subclasses of AGN into two populations: Population A-B separated at $\text{FWHM}(\text{H}\beta) = 4000 \text{ km s}^{-1}$. Physical drivers for the correlation were discussed in Marziani et al. (e.g. 2003) with black hole mass and Eddington ratio L/L_{Edd} (where $L_{\text{Edd}} = 1.5 \times 10^{38} (M/M_{\odot})$ is the Eddington Luminosity) identified as the principal drivers of change along the 4DE1 sequence. Black hole mass increases from Pop. A to Pop. B while Eddington ratio decreases from Pop. A to Pop. B.

The division into two populations is, at the least, useful for highlighting major differences among Type 1 AGN, although spectral differences among objects within the same

population are still noticeable, especially for Pop A sources (Figure 2 of Sulentic et al. 2002). This is the reason why they also divided the 4DE1 optical plane into bins of $\Delta\text{FWHM}(\text{H}\beta) = 4000 \text{ km s}^{-1}$ and $\Delta R_{\text{FeII}} = 0.5$. Bins A1, A2, A3, A4 are defined in terms of increasing R_{FeII} , while bins B1, B1⁺, and B1⁺⁺ are defined in terms of increasing $\text{FWHM}(\text{H}\beta)$ (see Fig. 1 of Sulentic et al. 2002). Sources belonging to the same spectral type show similar spectroscopic measures and physical parameters (e.g. line profiles and UV line ratios). Systematic changes are minimized within each spectral type so that an individual quasar can be taken as representative of all sources within a given spectral bin. The binning adopted in Sulentic et al. (2002) is valid for low z (< 0.7) quasars. At higher z an adjustment must be made since no sources with $\text{FWHM}(\text{H}\beta) < 3500 \text{ km s}^{-1}$ are found above redshift $z \sim 3$ (Marziani et al. 2009).

2. The targets

In this study we choose two representative examples of extreme Pop. A objects which show prominent $\text{AlIII}\lambda 1860$ and weak/absent $\text{CIII]}\lambda 1909$ emission lines. The objects are: the low redshift ($z = 0.06$) NLSy1 prototype I Zw 1 and the much more distant ($z = 3.23$) SDSS J120144.36+011611.6 that appears to be a prototype of higher redshift NLSy1-like sources. Both are shown in Fig. 1. Sources like I Zw 1 are found at intermediate to high redshift. Interpreted as the youngest and highest accreting sources (Sulentic et al. 2000) we might well expect to find more of them at high z . SDSS J12014+0116 is a good example of a high-redshift, high-luminosity analog of I Zw 1 with broader lines (as can be seen in the right panels of Fig. 2 where we show the line fits and can identify the broad component (BC) width of each object). In this paper, we shall use the acronym BC for this core or central component only. The spectrum of SDSS J12014+0116 shows lines that have $\text{FWHM}(\text{BC}) \sim 4000 \text{ km s}^{-1}$ which is much broader than the nominal NLSy1 cutoff of 2000 km s^{-1} at low redshift. Emission line ratios (such as $\text{AlIII}\lambda 1860/\text{SiIII]}\lambda 1892$, that can be derived from Table 2) and hence inferred physical conditions, are very close to those inferred for I Zw 1. This extends to other properties such as strong iron emission and a large blue asymmetric/blueshifted component of $\text{CIV}\lambda 1549$ (extreme Pop. A objects in Sulentic et al. 2007). Thus the “NLSy1 definition” seems to be luminosity dependent (see also Netzer & Trakhtenbrot 2007, Marziani et al. 2009) in the sense that we can extend this definition to high-luminosity and high redshift objects by extending the line widths limit to 4000 km s^{-1} and leaving all other properties unchanged (Dultzin et al. 2011).

A search in the SDSS DR7 for quasars in the redshift range where both $\text{CIV}\lambda 1549$ and the $\text{H}1900\text{\AA}$ blend are observed at optical wavelengths ($2 \lesssim z \lesssim 3$) yields more than 200

sources (out of 3000 candidates) with spectra resembling I Zw 1 on the basis of AlIII λ 1860 emission line strength (comparable to SiIII λ 1892). In practice, we performed automatic measurements of the spectra, measuring a rough approximation of the AlIII λ 1860/SiIII λ 1892 intensity ratio. As approximate as these measurements are, they are nonetheless suitable for identifying strong AlIII λ 1860 emitters. SDSS J12014+0116, is a prototype of these strong AlIII λ 1860 emitters selected on the basis of moderate/high S/N.

In summary, both at low- and high- z , as well as at low- and high-luminosity, around 10% of quasars are I Zw 1-like (i.e. NLSy1 type) on the basis of their emission line strengths. Particularly strong AlIII λ 1860 emission is observed in SDSS J12014+0116 with almost the same intensity as SiIII λ 1892. It also shows weak CIII λ 1909 (discussed in §3.2.2). In this paper we limit and justify the application of our method to NLSy1s which comprise around 10% of quasars. In a forthcoming paper, we shall address the applicability of our method to broader line quasars of both populations A and B.

3. Observations and Data Analysis

We retrieve the UV spectrum of I Zw 1 (upper panel of Fig. 1), obtained with the FOS spectrograph, from the HST archives². This instrument had a spectral resolution of about 1300 over the 1150 Å to 8500 Å range. The spectrum covers the range from 1150 to 3000 Å with S/N of ~ 45 around 1900Å. The SDSS J12014+0116 spectrum (lower panel of Fig. 1) covers the rest frame range from 1000 to 2100 Å with S/N of ~ 30 around 1900Å. This spectrum was taken from the SDSS DR7 site within the the *Legacy* project³. The spectroscopy in this project covers a wavelength range from 3800 to 9200 Å range with spectral resolution of 1800-2200.

3.1. Methodological considerations

In order to deblend and identify the principal lines, as well as to extract the core of the broad emission lines, we use the following previous results:

- As mentioned above, (Sulentic et al. 2002) divided Pop. A and B sources into bins according to FWHM H β and R_{FeII} measures. In 2010, Zamfir et al. computed median

²It can be retrieved from the Web site at <http://archive.stsci.edu>

³For more information about the *Legacy* survey, see the SDSS Web site at <http://www.sdss.org>

composite $H\beta$ spectra for each of the bins and showed that the broad $H\beta$ profiles in composite spectra of Population A sources are best fit by Lorentzian functions. In Population B objects, on the other hand, they are best described by Gaussian profiles (see also Marziani et al. 2010). This is an empirical result clearly shown in these works. Our sources are extreme Pop. A objects (bin A3) and thus we shall use Lorentzian profiles to model the broad components.

- Marziani et al. (2010) analyze 6 sources (including I Zw 1) representative of the six most populated bins of populations A and B. They show that FWHM and profile shape of broad components of $\text{SiIII}\lambda 1892$, $\text{AlIII}\lambda 1860$ and $\text{CIV}\lambda 1549$ are similar to those of $H\beta$. We do not have an $H\beta$ spectrum for SDSS J12014+0116 since there are no near IR data for this object. However for other high z quasars, there are high S/N IR spectra (Sulentic et al. 2004) that show NLSy1-like sources (defined in §2), with $M_B = -28$ and $\text{FWHM}(H\beta)$ as much as 2000km s^{-1} broader than those with $M_B = -22$. SDSS J12014+0116 shows $M_B = -29.8$ with $\text{FWHM}\sim 4000\text{km s}^{-1}$ while for I Zw 1 $M_B = -23.5$ and $\text{FWHM}\sim 2000\text{ km s}^{-1}$. With larger samples at high redshift (e.g. Marziani et al. 2009) the result that the $\text{FWHM}(H\beta)$ can be as high as 4000 km s^{-1} for NLSy1-like objects is confirmed. Following these results we use a Lorentzian profile with the same width ($\text{FWHM}\sim 4000\text{ km s}^{-1}$ in SDSS J12014+0116 and $\text{FWHM}\sim 2000\text{ km s}^{-1}$ in I Zw 1) for all the BCs of the broad emission lines.
- HIL $\text{CIV}\lambda 1549$ profiles show significant differences between Pop. A and B sources. In Pop. A. the peak of the line is often blueshifted and the profile blue asymmetric. We model this as a strongly blueshifted ($\lesssim -1000\text{ km s}^{-1}$) $\text{CIV}\lambda 1549$ broad component (hereafter labeled BLUE; Sulentic et al. 2007) plus an unshifted broad component analogous to the one seen in $H\beta$. We assume that the profile of this blueshifted component is Gaussian as discussed in Marziani et al. (2010).
- In Pop. A objects, low ($\text{SiII}\lambda 1814$) and intermediate ($\text{AlIII}\lambda 1860$, $\text{SiIII}\lambda 1892$) ionization lines offer the simplification of showing only the broad component associated with low-ionization emission (Marziani et al. 2010).

All the above results are taken into account for modeling the lines in this paper.

3.2. Measurements

After identifying the emission lines needed for our study, we isolate the broad central component in each of them using spectral decompositions as explained below. We need the

line fluxes to obtain n_{H} and U , the rest-frame specific flux at 11700\AA to compute r_{BLR} and the FWHM of the broad components to estimate M_{BH} . We use the SPECFIT IRAF task (Kriss 1994) that enables us to fit the continuum, emission and absorption line components, as well as FeII and FeIII contributions. We work with emission lines in the spectral range $1400 - 2000\text{\AA}$ which have been studied in great detail in both high and low- z quasars and where identification of prominent resonance and inter-combination lines is well established.

The steps we followed to accomplish identification, deblending and measurement of lines in each object were the following:

1. The continuum. We adopted a single power-law fit to describe it (Figure 1) using the continuum windows around 1700 and 1280\AA (see e.g. Francis et al. 1991). FeII emission in these ranges is weak leading us to assume that continuum measurement in those windows is reliable enough for our method (within the uncertainties, see §3.2.1).

2. BC line widths and shifts. We assume that a single value of FWHM (last Column of Tab. 2) is adequate to fit the BCs of all lines. BC shifts of all lines are the same and consistent with the redshift reported in the Table. Due to the fact that the CIII] λ 1909 emission line is mostly emitted in a different region than the rest of the broad lines (see discussion in §3.2.2) we do not impose the same restriction on the FWHM of CIII] λ 1909.

3. 11900\AA blend. In Table 1 we summarize the properties of the strongest features expected that contribute to the 11900\AA blend. Col. (1) lists the ion. Col. (2) is the rest frame wavelength. Col. (3) and (4) lists the the ionization potential and energy levels of the transition respectively. Col. (5) gives the configuration of the levels for the transition. Col. (6) and (7) give the transition probabilities and critical densities respectively. And in Col. (8) we give some notes for each ion. Forbidden lines of Si and C are not expected to be significantly emitted in the BLR and will not be further considered.

FeIII lines are frequent and strong in the vicinity of CIII] λ 1909 as seen in the SDSS template quasar spectrum (Vanden Berk et al. 2001). They appear to be strong when AlIII] λ 1860 is also strong (Hartig & Baldwin 1986). They are included in the photoionization simulations described below (Sigut et al. 2004). Ly α pumping enhances FeIII] λ 1914.0 (UV 34, Johansson et al. 2000) and this line can be a major contributor to the blend on the red side of CIII] λ 1909. The spectrum of I Zw 1 convincingly demonstrates this effect: both CIII] λ 1909 and FeIII] λ 1914 are needed to account for the double peaked feature at 1910\AA

that is too broad to be explained by a single line (Fig. 2).⁴ We adopt the template (option B) of Vestergaard & Wilkes (2001) plus additional FeIII λ 1914, with the same profile as the other BCs lines, for modeling FeIII emission in our sources.

FeII emission is not strong in the spectral range we studied and the UV FeII template we adopt is based on a suitable CLOUDY simulation. Results on the H1900Å blend are not significantly affected by the assumed FeII contribution since it appears as a weak pseudo-continuum underlying the blend. We explore maximum and minimum contributions of FeII by placing the highest and lowest possible continua, as shown in Fig 1, and as explained below in §3.2.1. In Figure 2 we show the contribution of FeII. If we increase or decrease this contribution, we will see an intensity variation of the strength of the lines, being SiII λ 1814 the most affected due its weakness (see error bands in Fig. 6). We take into account this strength variations for the error estimations.

Then, for both objects, we sequentially model FeII and FeIII as preliminary steps. We anchor the FeII template to the 1785 Å feature in order to normalize it. We continue with the fit of the SiII λ 1814 and AlIII λ 1860 emission lines that are fairly unblended. The main challenge is therefore to deconvolve SiIII] λ 1892, CIII] λ 1909, and FeIII λ 1914, noting that we will use only the less blended line, SiIII] λ 1892, for the eventual computation of diagnostic ratios.

The next step is different for each object. The deblending of SiIII] λ 1892, CIII] λ 1909, and FeIII λ 1914 can be easily accomplished in the case of I Zw 1 because the lines are narrow. In the case of SDSS J12014+0116 the peak at H1910 is consistent with FeIII λ 1914 indicating that FeIII emission is dominating over CIII] λ 1909. Thus, we first fit SiIII] λ 1892 and FeIII λ 1914 to the observed peaks and the remaining part of the blend, as CIII] λ 1909. We emphasize that in the H1900Å blend, the only two lines that are severely blended are CIII] λ 1909 and FeIII λ 1914. This is more evident in the case of I Zw 1 because CIII] λ 1909 and FeIII have similar intensities. In the case of SDSS J12014+0116, CIII] λ 1909 is much weaker than FeIII λ 1914 but still blended. We are not interested in the intensity of these two lines but only in a confirmation that CIII] λ 1909 is weak with respect to SiIII] λ 1892. In Figure 3 we show that this is valid even for the highest possible contribution of CIII] λ 1909. The residuals in Figures 2 and 3 reflect the noise. If we consider 1σ above and below zero, then we say that a line is weak when it is below 1σ . For example, in the lower right panel of Fig. 2, CIII] λ 1909 is below 1σ , while SiII λ 1814 is around 1.5σ .

⁴Note that the Galactic line of Mg I at 2026 Å can contribute to the split appearance of the redshifted H1910 Å feature (Fig. 2). This absorption line is included in the SPECIFY analysis, but its resulting equivalent width is very small. The line separation between CIII] λ 1909 and FeIII λ 1914 is mostly intrinsic.

4. H1550 Å feature. As in the case of the previous blend, we need to keep in mind the complexity of this feature. In order to fit the HIL C^{IV}λ1549, we have to take into account that it is decomposed into a Lorentzian BC with the same width and shifts of the intermediate ionization lines plus a blueshifted residual (assumed to be Gaussian in the SPECFIT procedure, discussed in §3.1). So, in both objects, we fit first the FeII template with the same intensity as in the H1900Å blend. Then we fit the BC, and looking at the residuals, we fit the BLUE component. Finally, we fit the underlying weaker emission lines N^{IV}λ1486, SiIIλ1533 and HeIIλ1640, when visible. We assume that the latter line has two components (BC and BLUE) with the same shift and width as C^{IV}λ1549. An equivalent approach has been successfully followed by several authors (Baldwin et al. 1996; Leighly & Moore 2004; Marziani et al. 2010; Wang et al. 2011).

We need to point out that in the case of I Zw 1, we observed a narrow component (NC) with a width of $\sim 800 \text{ km s}^{-1}$, close to the width to the BCs of the broad lines. The NC of C^{IV}λ1549 is observed in several low-*z* quasars (also radio loud) and Seyfert-1 nuclei, as well as in type-2 quasars (Sulentic et al. 2007). Even if the line is collisionally excited (hence with an intensity proportional to the square of electron density), the larger volume of the narrow line region (proportional to $(R_{NLR}/R_{BLR})^3$) and the absence of collisional quenching at a relatively low density (as in the case of the [OIII]λλ4959,5007 lines) make it possible to expect a significant C^{IV}λ1549 NC emission. We also observed that for I Zw 1, the NC of C^{IV}λ1549 is blueshifted. This is also observed in other narrow lines (Marziani et al. 2010), in agreement with expectations for the NLR of the extreme NLSy1s. For example, [OIII]λλ4959,5007 is blueshifted with respect to Hβ and to the systemic radial velocity of the host galaxy. In this way the analysis of the C^{IV}λ1549 NC is fully consistent with the [OIII]λλ4959,5007 and Hβ analysis.

5. H1400 Å blend. This blend has been one of the most enigmatic features in quasar spectra (e.g., Wills & Netzer 1979). It is known that the Si^{IV}λ1397 doublet is blended with O^{IV} intercombination lines (Nussbaumer & Storey 1982). In our sources the H1400Å blend is very prominent, approximately 3-4× stronger relative to C^{IV}λ1549 than in the SDSS composite quasar spectrum (Vanden Berk et al. 2001). This is consistent with the extreme metal enrichment we found in these sources (§6.1.1).

We are able to obtain a reliable measurement of the Si^{IV}λ1397 doublet, even when we cannot measure all the components of the H1400Å blend. Any O^{IV}λ1402 contribution to the BCs is expected to be negligible ⁵. We follow the same procedure to fit this blend as in

⁵This is not true for the BLUE component. The physical properties derived for the BLUE component

11550Å blend. Note that the SiIVλ1397 low-ionization emission line shows a double horned profile in I Zw 1 because of the large doublet separation and of the relatively narrow lines of this source. Since the peak at ≈ 1401 Å is somewhat broader than the peak of the individual component of SiIVλ1397, some OIV]λ1402 emission might be associated to the O III]λ1663 emitting region. This is an additional, minority component that is needed to obtain a very good fit of the 1400Å blend.

In summary, the three following features were independently fitted (using SPECFIT, see Fig. 2):

The 1400 Å blend (whose profile is very similar to the one of CIVλ1549), with BC of SiIVλ1397 (we fit the doublet with individual lines at 1402 and 1394 Å), and one blueshifted component accounting for the contribution of both SiIVλ1397 and OIV]λ1402 (+ semi-broad component most probably associated to OIV]λ1402 in I Zw 1).

The 1550 Å feature, with CIVλ1549 BC + BLUE + FeII + Si III]λ1531. We expect a contribution of HeIIλ4686 with a profile similar to CIVλ1549. In SDSS J12014+0116 we can see HeIIλ4686 BLUE.

The 1900 Å blend considering FeII, FeIII, SiIIλ1814, AlIIIλ1860 (we fit the doublet with independent lines, at 1855 and 1862 Å, in Fig. 2 we show only the sum), SiIII]λ1892, CIII]λ1909 and FeIII]λ1914. This latter line is assumed to be an independent additional line of unknown intensity and with the same profile as the other BCs.

All BCs of the broad emission lines are assumed to have the same width and shift, leaving only their intensity as free parameters. The HIL blends involve mainly only two components. As a result, the free parameters are reduced to the intensity of the BC lines (CIII]λ1909, SiIII]λ1892, AlIIIλ1860, SiIIλ1814, CIVλ1549 and SiIVλ1397), the intensity of the FeII and FeIII templates and the width and flux of the Gaussian minor components under CIVλ1549 (NIV]λ1486, SiIIλ1533, HeIIλ1640) and SiIVλ1397 (OIV]λ1402). Table 2 reports the fluxes of the BCs for intermediate and high ionization lines. Col. (1) is the object name. Col. (2) is the redshift, for I Zw 1 we adopted the one reported in Marziani et al. (2010); for the SDSS J12014+0116 object we use one reported in the SDSS database. Col. (3) is the

($0 \gtrsim \log U \gtrsim -1$, $\log n \lesssim 9$, Leighly 2004; Marziani et al. 2010) indicate that both SiIVλ1397 and OIV]λ1402 should contribute to the BLUE intensity.

rest-frame specific flux at 11700\AA . Cols. (4) to (9) are the rest-frame line flux for the broad components only, and Col. (10) is the FWHM of all the broad components.

3.2.1. Uncertainties

The main sources of uncertainties in the measurements are the following:

FeII intensity (continuum placement). Broad FeII emission can produce a pseudo-continuum affecting our estimates of emission line intensities. SiII λ 1814 is especially affected in our spectra because it is weak (Fig. 1). The effect is less noticeable for CIV λ 1549 and SiIV λ 1397, since the expected FeII emission underlying those lines is weak. The placement of this pseudo continuum also affects the determination of r_{BLR} for which we use the continuum flux measured at 11700\AA (see column 3 of Table 2 and equation 8).

FeIII intensity. These multiplets affect mainly the intensity of the CIII] λ 1909 emission line. We measured the maximum and minimum possible contributions of CIII] λ 1909 depending on the intensity of FeIII λ 1914. The contribution of CIII] λ 1909 has no considerable effect to the intensity of SiIII] λ 1892 even in the case were FeIII λ 1914 is maximum. This is important for the case of the SDSS object. In order to reproduce the observed 11900\AA blend, if we increase the intensity of the CIII] λ 1909 emission line, the intensity of FeIII λ 1914 necessarily has to decrease and viceversa. As a result SiIII] λ 1892 is not really affected by these variations. As a result the line intensity of SiIII] λ 1892 is affected only by about $\sim 10\%$, which is within the uncertainties, as shown in Table 2. In the lower right panel of Fig. 2 and in Fig. 3 we show the maximum and minimum contributions of CIII] λ 1909 and FeIII λ 1914.

BLUE component. In the case of the CIV λ 1549 and SiIV λ 1397 emission lines, the main source of error is the contribution of the BLUE component on the blue side of the central component. To a less extent, we may have a BLUE component contribution of HeII λ 4686 on the red side of CIV λ 1549. In the previous section we describe how we deal with these contributions.

FWHM. When we run the SPECFIT routine we set the same FWHM for all the BCs of the broad emission lines. However, the routine introduces slight fluctuations around this initial value in order to obtain the best fit. When we vary the placement of the continuum, the

FWHM determination is also affected. This source of error is reflected in the computation of the M_{BH} .

3.2.2. CIII] λ 1909 emission

One must work carefully with the 1900Å blend because of the close proximity of the CIII] λ 1909, FeIII]1914 and SiIII] λ 1892 emission lines. Both of our targets are extreme Pop. A sources and one characteristic of this extreme population is that CIII] λ 1909 is weak or even absent (Fig. 2). Extreme Pop. A sources show the lowest CIII] λ 1909/SiIII] λ 1892 ratio among all quasars in the E1 sequence (Bachev et al. 2004). We can see this effect in the upper right panel of Figure 2 where we show the 1900Å blend for I Zw 1. The resolution is good enough to separate the peaks of FeIII]1914 and CIII] λ 1909. After fitting the FeIII template (including the FeIII]1914 line), we see that in order to fit the observed spectrum the intensity of the CIII] λ 1909 line turns out to be comparable to FeIII]1914. In the right lower panel, for the SDSS J12014+0116 object, the spectrum is noisier and the peaks of the lines of CIII] λ 1909 and FeIII]1914 are not clearly seen. However, the observed peak is at the position of FeIII]1914, and if we follow the same procedure to fit the FeIII template in order to deconvolve the blend, it turns out to that the contribution of the CIII] λ 1909 emission line is practically insignificant. To estimate an upper limit to the CIII] λ 1909 line, we remove FeIII]1914 (Fig. 3). This estimate is CIII] λ 1909 \approx 0.5 SiIII] λ 1892 for the SDSS J12014+0116 object, but the fit is poor on the red side of the blend leaving a large residual. In order to minimize the residual we added the maximum possible contribution of CIII] λ 1909 emission line (Fig. 3) We can safely conclude that CIII] λ 1909/SiIII] λ 1892 $<$ 0.5 in this object. CIII] λ 1909 emission line in I Zw 1 is about \approx 0.6 SiIII] λ 1892. The very dense region emitting the LILs should produce no CIII] λ 1909 line because it is collisionally quenched; so any emission from this line should arise in a different region.

Available reverberation mapping results suggest that CIII] λ 1909 line is mainly emitted farther out from the central continuum source than some LILs and HILs. The results of reverberation mapping analysis are limited to a handful of low luminosity objects and cannot be generalized in a straightforward way. However, in these low luminosity objects CIII] λ 1909 line responds to continuum changes on timescales much longer than CIV λ 1549 and other HILs. This results comes from the analysis of total CIII] λ 1909 + SiIII] λ 1892 in NGC 3783 (Onken & Peterson 2002), from the CIII] λ 1909 of NGC 4151 (Metzroth et al. 2006) and of NGC 5548. It is intriguing that the CIII] λ 1909 cross-correlation delay in NGC 5548 (by far the best studied object) is even larger than that of H β (32 ld vs. 20 ld; Peterson et al. 2002; Clavel et al. 1991). For fixed density, lines of higher ionization form at higher photon

flux. The C^{++} , Al^{++} , Si^{++} ionization potential are 24, 18, and 16 eV respectively. These comparable ionization potentials are well below the one of HILs, $X^{i-1} \gtrsim 50$ eV. However, the much lower $C\text{III}]\lambda 1909$ critical density implies that the $C\text{III}]\lambda 1909$ line should be formed farther out than $Si\text{III}]\lambda 1892$ and $Al\text{III}]\lambda 1860$ if all these lines are produced under similar ionization conditions.

We also want to point out that there are plausible physical scenarios that can give rise to $C\text{III}]\lambda 1909$ in a shielded, non-uniform environment where there gas has a range of densities at similar ionization parameter (i.e., the less dense gas is somehow shielded; Maiolino et al. 2010). Since we are considering profiles integrated over the whole unresolved emitting region, the relevant question is however: how much will the $C\text{III}]\lambda 1909$ emitting regions contribute to the lines we are considering? The strongest $C\text{III}]\lambda 1909$ emitters along the E1 sequence (spectral type A1) typically show $C\text{III}]\lambda 1909/Si\text{III}]\lambda 1892 \approx 2.5$. Kuraszkiwicz et al. (2004) more typically found $C\text{III}]\lambda 1909/Si\text{III}]\lambda 1892 \approx 5$. The results of the fits indicate that $C\text{III}]\lambda 1909$ emission is very weak respect to $Si\text{III}]\lambda 1892$ in our spectra. We obtain $C\text{III}]\lambda 1909/Si\text{III}]\lambda 1892 \approx 0.6$ for I Zw 1 and $C\text{III}]\lambda 1909/Si\text{III}]\lambda 1892 \approx 0.2$ for SDSS J12014+0116. Therefore the results of our procedure (described in §3.2) will not be significantly affected. If the ionization parameter is $\log U \lesssim -2.5$, there will be modest HIL emission. Other intermediate ionization lines will be little affected. The results of the fits indicate that $C\text{III}]\lambda 1909$ emission is low. We therefore neglect the effect of any $C\text{III}]\lambda 1909$ emitting gas on the intermediate and high ionization lines.

4. Definition of Diagnostic Ratios and their Interpretation

4.1. Definition

Our method for estimating n_H and U involves several line ratios. We discuss the product $n_H \cdot U$ in the following sections and in §6.2 we use it to compute r_{BLR} . We define three groups of diagnostic ratios which should define density, ionization parameter, and metallicity for a given continuum shape and geometry.

Line ratios such as $Al\text{III}]\lambda 1860/Si\text{III}]\lambda 1892$ are useful diagnostics over a range of density that depends on their transition probabilities. Emission lines originating from forbidden or semi-forbidden transitions become collisionally quenched above the critical density and therefore relatively weaker than lines for which collisional effects are still negligible. The $Al\text{III}]\lambda 1860/Si\text{III}]\lambda 1892$ ratio is well suited to sample the density range $10^{11} - 10^{13} \text{ cm}^{-3}$. This corresponds to the densest emitting regions likely associated with production of LILs like the $Ca\text{II}$ IR triplet (Matsuoka et al. 2008) and $Fe\text{II}$ (Baldwin et al. 2004).

The ratios $\text{SiII}\lambda 1814/\text{SiIII}\lambda 1892$ and $\text{SiIV}\lambda 1397/\text{SiIII}\lambda 1892$ are sensitive to ionization, but roughly independent of metallicity since the lines come from different ionic species of the same element. Metallicity influences thermal and ionization conditions that in turn affect these ratios. The effect is however second-order: CLOUDY simulation sets for different Z indicate that, for a fivefold increase in metal content the ratio $\text{SiIV}\lambda 1397/\text{SiIII}\lambda 1892$ changes from ≈ 0.5 to 0.6.

The ratio $\text{SiIV}\lambda 1397/\text{CIV}\lambda 1549$ is mainly sensitive to the relative abundances of C and Si. The reason is that the ground and excited energy levels of these ions are very similar (the ionization potentials are close: 33.5 and 48 eV for creation of Si^{+3} and C^{+3} , respectively). This implies that the dependence on continuum shape and electron temperature of the ratio of this two resonance lines is small (see also Simon & Hamann 2010).

4.2. Interpretation

In order to illustrate how we employ CLOUDY simulations to estimate where the bulk of the line emission arises we refer to Figure 4. The left panel shows the ionic fraction as a function of geometrical depth in a slab (within a single BLR cloud) for which we choose a fixed column density⁶ ($N_c = 10^{25} \text{ cm}^{-2}$) and density ($n_H = 10^{12.5} \text{ cm}^{-2}$) exposed to a “standard” quasar continuum (the parameterization of Mathews & Ferland 1987). It is customary to consider this parameterization as standard for the ionizing continuum. However, that parameterization has been sometimes criticized and it is not unique, so that we also consider as an alternative the ionizing continuum parameterization of Laor et al. (1997b). In this work, we use the term ‘typical continuum’ to designate the average of the two, with the two continua providing two extrema in number of ionizing photons expected at a specific flux measured on the non-ionizing part of the continuum. The ‘typical continuum’ is the one used for our computation of r_{BLR} (see §6.2).

Computing simulations at a fixed n_H and U values allows us to study how these parameters influence the diagnostic ratios we have defined. We make no assumptions about the geometry or kinematics of the BLR. The slab of gas (i.e. a single cloud) might as well involve magnetically confined clouds (Rees et al. 1989) or individual elements in an accretion disk

⁶The value of $N_c = 10^{25} \text{ cm}^{-2}$ was needed to show that the Strömgen depth is less than the size of the clouds for the ionic states we are considering, i.e., that clouds are radiation bounded. In Figure 4 we show that if we assume $N_c = 10^{25} \text{ cm}^{-2}$, the clouds become optically thick to electron scattering and we use them just to show the ionization structure and the line emissivity. Fig. 4 reproduces also the structure and emissivity of a typical $\log N_c = 10^{23}$ slab (in this case the limit of geometrical depth is $\log h \approx 10.5$).

atmosphere – provided that photoionization is the only heating mechanism.

Al⁺⁺, Fe⁺⁺, and Si⁺⁺ are intermediate ionization lines sharing a region of dominance deep within a cloud – where the HILs are also arise. It is therefore appropriate to consider intermediate-ionization line ratios between geometric depths $h \sim 10^6 - 10^8$ cm (right panel of Figure 4). We prefer to show the product of the local line emissivity times the depth within the slab since the total line intensity is proportional to $\int \epsilon(h)dh$ (in the absence of radiation transfer effects i.e., in a cloud where lines are optically thin), and hence the product $\epsilon(h) \cdot h$ gives a better idea of the total line emission at a distance h than simply showing $\epsilon(h)$ vs. h . Fig. 4 shows that CIII]λ1909 emission is expected to be orders of magnitude lower than the other lines and therefore likely undetectable.

Once we have ascertained that the computed line ratios are physically consistent (i.e., all refer to a single emitting region except the ones involving SiIIλ1814, whose intensity is significantly affected by a partially ionized zone (PIZ) emission), a multidimensional grid of CLOUDY simulations is needed to derive estimates for U , n_H and metallicity from the spectral measurements (Ferland et al. 1998; Korista et al. 1997). CLOUDY computes population levels of the relevant ionic stages of Si, C, Al and, especially for lines emitted in the fully ionized part of a gas slab (Fig. 4). Also, CLOUDY is expected to be especially good for predicting intermediate and high ionization line fluxes that are produced in the fully-ionized region within the gas slab. Low ionization lines are produced in the PIZ by photoionization of hydrogen –primarily by soft X-ray photons. Since these X-ray photons create supra-thermal electrons and have a relatively low cross section for photoionization, the heating processes in the PIZ are inherently non-local, making the mean escape probability formalism used by CLOUDY to treat radiation transfer a very rough approximation.

New simulations were needed since CLOUDY has undergone steady and significant improvements since the time of Korista et al. (1997). The most relevant improvement is the addition of more ionic species in the simulations, with a 371-level of the Fe⁺ ion. This will make computation of equilibrium conditions more realistic even if, in the end, we expect that predictions of line intensity ratios will not be dramatically affected: iron is singly ionized only in the PIZ (Fig. 4, left panel). Other relevant improvement for our study is the post-Korista et al. (1997) update of the transition probability for SiIIλ1814 following Callegari & Trigueiros (1998) that changes the intensity of the line by a factor of ~ 2 in the high density regime of the BLR. We present the results of our simulations in Figure 5. Our results are not inconsistent with those obtained by Korista et al. 1997, for the same ranges of density and ionizing parameter: the overall behavior in the plane (U , n_H) of their Figure 3 is qualitatively consistent with the one derived from our simulations.

Simulations assume: (1) pure photoionization (see also §6.1) and (2) spherical symme-

try in continuum emission, i.e. that the ionizing continuum incident on a slab of gas of fixed density is similar to the observed continuum (see §6.2.1 for caveats concerning this assumption).

The ionization state of the gas will be mainly defined by the ionization parameter:

$$U = \frac{\int_{\nu_0}^{+\infty} \frac{L_\nu}{h\nu} d\nu}{4\pi n_H c r^2} \quad (1)$$

where L_ν is the specific luminosity per unit frequency, h is the Planck constant, ν_0 the Rydberg frequency, n_H the hydrogen density, c the speed of light, and r is the distance between the central source of ionizing radiation and the line emitting region.

Simulations span the density range $7.00 \leq \log n_H \leq 14.00$, and $-4.50 \leq \log U \leq 00.00$, in intervals of 0.25 assuming of plane-parallel geometry. We assume the standard value of $N_c = 10^{23} \text{ cm}^{-2}$ (Netzer & Marziani 2010, and references therein). In Figure 5 we show the isocontours for the ratios $\text{AlIII}\lambda 1860/\text{SiIII}\lambda 1892$, $\text{SiII}\lambda 1814/\text{SiIII}\lambda 1892$, $\text{SiIV}\lambda 1397/\text{SiIII}\lambda 1892$, $\text{CIV}\lambda 1549/\text{AlIII}\lambda 1860$, $\text{CIV}\lambda 1549/\text{SiIII}\lambda 1892$ and $\text{SiIV}\lambda 1397/\text{CIV}\lambda 1549$ derived from CLOUDY simulations, for solar metallicity and “standard” quasar continuum, as parameterized by Mathews & Ferland (1987) (see above). We considered three chemical compositions: (1) solar metallicity; (2) constant abundance ratio Al:Si:C with $Z = 5Z_\odot$; (3) an overabundance of Si and Al with respect to carbon by a factor 3, again with $Z = 5Z_\odot$ ($5Z_\odot \text{SiAl}$). This last condition comes from the yields listed for type II Supernovæ (Woosley & Weaver 1995). The Si overabundance is also supported by the chemical composition of the gas returned to the interstellar medium by an evolved population with a top-loaded initial mass function simulated using STARBURST99 (Leitherer et al. 1999). The abundance of Al is assumed to scale with the one of Si (see also §6.1 on this assumption).

5. Results

5.1. Density and Ionization Parameter

In this section, we compute the ratios analyzed above from the flux values and we estimate the physical parameters n_H and U of the BLR, for I Zw 1 and SDSS J12014+0116. We derived these values from the emission lines measurements, reported in Table 2, and the CLOUDY simulations of Figure 5. Asymmetric errors due to the uncertainties described in §3.2.1, have been quadratically propagated following Barlow (2003, 2004).

In left panels of Figure 6 we show the same n_H vs U plane as in Figure 5 (in right panels, we use the $5Z_\odot \text{SiAl}$ simulation defined above). We choose only one isocontour for each ratio,

and it is the one that corresponds to the measured value. There is convergence of the contours lines defined by several crossing-points of the contour of the $\text{AlIII}\lambda 1860/\text{SiIII}\lambda 1892$ ratio versus the contour of the other 5 ratios. This convergence defines the n_{H} and U values that point towards a low ionization plus high density range. We use the average value of all of the crossing-points to define a single $n_{\text{H}}\cdot U$ value, which is used to compute the r_{BLR} and the M_{BH} (§6.2).

The uncertainties associated to a line ratio, R , broaden the lines defined by constant R to a band limited by the ratios $R \pm \delta R$. In Fig. 6, we show them with bands. The largest of all uncertainties is related to $\text{SiII}\lambda 1814$. This is the weakest line that we use and thus it is the line most strongly affected by the continuum placement. The value of $\text{SiII}\lambda 1814$ intensity is probably underestimated, and if it was higher, the crossing point of $\text{AlIII}\lambda 1860/\text{SiIII}\lambda 1892$ vs $\text{SiII}\lambda 1814/\text{SiIII}\lambda 1892$ would be closer of the other crossing points, marked by an arrow in Fig. 6. We stress also that $\text{SiII}\lambda 1814$ is the only low-ionization line considered in this study, and its formation is sensitive to the assumed X-ray continuum and other LIL-formation issues (Dumont & Mathez 1981; Baldwin et al. 1996).

The discrepancy in the intersection point of diagnostic ratios in the plane (n_{H} , U) is significant for the $\text{SiIV}\lambda 1397/\text{CIV}\lambda 1549$ ratio that depends mainly on the Si abundance relative to C. The $\text{H}1400/\text{CIV}\lambda 1549$ intensity ratio has been used as a metallicity indicator also by other authors (Juarez et al. 2009; Simon & Hamann 2010). The discrepancy is less but still significant for the case when we consider the $5Z_{\odot}\text{SiAl}$ case. For this reason, we do not consider this ratio in the computation of the product of density and ionization parameter.

In similar plots made for $Z = 5Z_{\odot}\text{SiAl}$ (right panels of Fig. 6), the agreement of all the crossing-points improves: the isocontour lines converge toward a better defined crossing-point.

The high metallicity case $5Z_{\odot}\text{SiAl}$ indicates higher U and smaller n_{H} with respect to the case of solar abundances, if emission line ratios involving $\text{CIV}\lambda 1549$ are considered. This reflects the increase in abundance of Si and Al relative to C with respect to solar: Si and Al lines appear stronger with respect to the $\text{CIV}\lambda 1549$ line because the elements Si and Al are more abundant, and not because a lower ionization level enhances $\text{SiII}\lambda 1814$, $\text{SiIII}\lambda 1892$, $\text{AlIII}\lambda 1860$ emission with respect to $\text{CIV}\lambda 1549$.

In the case of SDSS J1201+0116 we can see from Table 3 that the density is even higher than for I Zw 1, suggesting that $\text{SiIII}\lambda 1892$ is collisionally quenched to make possible a rather high $\text{AlIII}\lambda 1860/\text{SiIII}\lambda 1892$ ratio, ≈ 1 . The line intensity of $\text{SiIII}\lambda 1892$ is thus the result of the physical conditions of the emitting region, and in fact we measure a relatively low line intensity. The ratio $\text{AlIII}\lambda 1860/\text{SiIII}\lambda 1892$ has a value of 0.6 for I Zw 1.

5.2. The product (Un_{H})

The products ($n_{\text{H}} \cdot U$) derived from the Figure 6 and reported in Table 3 are marginally different for the two sources. It is intriguing, however, that while the values of n_{H} and U taken separately depend significantly on metallicity, their product shows a weaker dependence: for $Z = 1Z_{\odot}$, we obtain $\log(n_{\text{H}} \cdot U) \approx 9.4$ for I Zw 1 and 9.8 for SDSS J1201+0116. Similar results seem to hold also for a larger sample, including the objects monitored for reverberation mapping (Negrete 2011).

We also note that the $\log(n_{\text{H}} \cdot U)$ values are very close to the results of several independent, previous studies summarized in the Table 4.

Baldwin et al. (1996) presented a similar analysis. Their Fig. 2 organizes spectra in a sequence that is roughly corresponding to E1, going from $\text{AlIII}\lambda 1860$ - strong sources to objects whose spectra show prominent $\text{CIII]}\lambda 1909$ along with weak $\text{AlIII}\lambda 1860$ (Bachev et al. 2004). The line components they isolated correspond to the ones we consider in this paper: a blue-shifted feature, and a more symmetric, unshifted and relatively narrow component that we call LIL-BC. They derive $\log n_{\text{H}} \approx 12.7$ and $\log U \approx -2.5$. A somewhat lower density and higher ionization is indicated to optimize FeII emission, while the CaII IR triplet requires conditions that are very similar to the ones derived from the intermediate ionization lines.

We are not claiming that there is a single region that is able to account for all broad lines in all AGN. However, a low ionization, high density region can account for FeII , CaII and the intermediate ionization line emission. This region is dominating the BC of emission lines (save weak $\text{CIII]}\lambda 1909$) in the objects considered in this paper, but apparently becomes less relevant along the E1 sequence (Marziani et al. 2010). The properties of the emitting broad line region seem to be remarkably stable, keeping an almost constant $\log(n_{\text{H}} \cdot U)$ (also seen in previous work, e.g. Wandel et al. 1999, Baldwin et al. 1995). The issue is therefore whether we can apply the physical conditions (n_{H} and U) we deduce to derive information of r_{BLR} and M_{BH} .

6. Discussion

6.1. Alternative Interpretations

In this section we discuss other possible scenarios considering the influence of other sources of heating, besides photoionization. We again remark that, on the basis of the analysis of section §3, the use of intermediate and high ionization lines takes advantage of the most robust results of photoionization computations for AGNs. The complex issue of

LII formation is mostly avoided since we do not rely on the partially-ionized zone, whose physical properties may not be adequately modeled. Nonetheless, results on density stem mainly from the AlIII λ 1860 line being over-strong with respect to SiIII λ 1892. The observed AlIII λ 1860/SiIII λ 1892 line ratio is inconsistent with density $\sim 10^{11}$ cm $^{-3}$ that would make some CIII λ 1909 emission possible. Low ionization is inferred from the intrinsic weakness of CIV λ 1549 in these Pop. A sources with respect to CIV λ 1549, that is observed in Pop. B objects (Sulentic et al. 2007).

While there is little doubt about the identification of the AlIII λ 1860 line doublet (a resonance line with large transition probability; in several NLSy1s the doublet is resolved with ratio $\sim 1 - 1.2$, suggesting large optical depth), this line could be enhanced with respect to SiIII λ 1892 by some special mechanism. We can conceive two ways of increasing AlIII λ 1860 with respect to SiIII λ 1892: (1) a selective enhancement of the Al abundance with respect to Si, or (2) collisional ionization due to a heating mechanism different from photoionization.

6.1.1. Anomalous Chemical Composition

Evidence based on the strength of the NV λ 1240 line relative to the CIV λ 1549 and HeII λ 1640 lines, indicates that chemical abundances may be 5 to 10 times solar (Dhanda et al. 2007) in high redshift quasars, with $Z \approx 5Z_{\odot}$ reputed typical of high z quasars (Ferland et al. 1996). The [Si/C] enhancement (over solar) is supported by both STARBURST 99 simulations (Leitherer et al. 1999) and supernova yields (Woosley & Weaver 1995).

The production factors for progenitors reported by Woosley & Weaver (1995) indicate that there should be little [Al/C] enhancement for 11 – 20 M_{\odot} supernovae progenitors of solar metallicity of Z_{\odot} . Massive progenitors are needed to raise the [Al/C] enrichment as they are the most efficient producers of aluminium. We integrate the production factors over a top-loaded mass function $\Phi(M) \propto M^{-x}$. If $x = 1.3$ (for $M \leq 8 M_{\odot}$, a value held canonical for the initial mass function (IMF) of young star forming systems), we obtain production factors ratios of ≈ 3.0 and ≈ 2.5 for aluminium over carbon and silicon over carbon, respectively. We also try changing the high-mass end of the IMF. With $x = 2.1$, we obtain a factor of 2 enhancement for both aluminium and silicon. With $x = 1.1$, we obtain a significantly larger enhancement in aluminium than in silicon over carbon, with production factor ratios ≈ 3.5 and ≈ 2.7 . This condition is however rather extreme and the change in enrichment is rather small and will not affect significantly our diagnostic ratios.

The observed values are more consistent with the assumption of a starburst. A factor of ≈ 3 enhancement of Si and Al over C indicates that BLR is made of gas whose chemical

composition might reflect the enrichment due to a “young” starburst (\lesssim few 10^7 yr): a STARBURST 99 simulation indicates that ejecta from a stellar system formed in an instantaneous burst should be enriched in Si in between 2 and $4 \cdot 10^7$ yr.

6.1.2. Mechanical heating and FeII emission

NLSy1s of spectral type A3 and A4 are the sources for which pure photoionization models are deficient as far as the prominence of FeII emission is concerned (Joly et al. 2008). Since AlIII λ 1860 prominence correlates with FeII prominence along the E1 sequence, there might be a mechanical heating contribution to the thermal and ionization balance that is often invoked to explain FeII emission (Collin & Joly 2000; Baldwin et al. 2004). This second possibility reopens the issue of LIL formation that is too complex to be discussed in the present paper.

We can consider whether gas in collisional equilibrium at a fixed electron temperature could give rise to a spectrum accounting for the strong FeII λ 4570 and AlIII λ 1860 emission lines, as well as the line ratio SiIII] λ 1892/CIII] λ 1909 \approx 2 as observed in I Zw 1. We cannot ignore, however, that Balmer line emitting gas appears to be pre-eminently photoionized, also in NLSy1 objects, as convincingly demonstrated by several reverberation mapping campaigns, and that the width of FeII is consistent with the width of the H β rms spectrum (Sulentic et al. 2006a). Continuity arguments along the E1 sequence and monitoring studies indicate that photoionization cannot be fully dismissed. Also, I Zw 1 is among the strongest emitter along the E1 “main sequence” of Sulentic et al. (2000), but not an ultrastrong FeII emitter as defined by Lipari et al. (1993). Ultrastrong FeII emitters are outliers in the E1 optical plane (Sulentic et al. 2006b), and often ultra-luminous IR galaxies (ULIRGs) and extreme broad absorption line (BAL) sources. It is legitimate to suspect very different physical conditions in that case.

There is convincing evidence that FeII is responding to continuum changes, although measurements are very difficult and the response of FeII might be more erratic than H β (Vestergaard & Peterson 2005; Peterson 2011). PG 1700+518 is a strong FeII emitter, and monitoring of Fe II_{opt} indicates a response on a timescale consistent with the one obtained for H β (Bian et al. 2010; Peterson et al. 2004, note that Bian et al. 2010 are not able to derive a reverberation radius for H β , unlike previous monitoring campaigns). On the converse Akn 120, a source with significant FeII (Marziani et al. 1992; Korista 1992) shows a response that may be consistent with a region more distant than the one of H β , or with a region that is not photoionized (Kuehn et al. 2008). A recent work suggests that the large range of observed R_{FeII} values can be explained by photoionization, if the variation of iron abundance in dusty

gas is taken into account (Shields et al. 2010).

The (n_{H}, U) solution we find falls below the ionization level that maximizes FeII λ 4570 emission. Adopting the suggestion of S. Collin and collaborators (e.g. Joly 1987), a simulation computed in the case of a very weak photoionizing continuum and dominance of collisional ionization at $T = 7000\text{K}$, would enhance the R_{FeII} ratio to levels even in excess to the one observed, leaving however unaffected the intermediate and high ionization lines (since there are few electrons with energies sufficient to ionize their parent ionic species).

A system dominated by collisions at a fixed, single temperature higher than $\approx 10000\text{K}$ would yield contradictory results. For example, a collisional equilibrium solution at $T = 20000\text{K}$ and $\log n_{\text{H}} = 10$ would imply R_{FeII} exceeding by a factor 2 the observed value. Ratios involving the AlIII λ 1860, SiIII λ 1892 and SiIV λ 1397 emission lines would be consistent with the observed ones, but the solution overpredicts the intensity of intermediate ionization emission lines by a factor ~ 100 , with little CIII λ 1909 and no CIV λ 1549. If any such region exists, it must contribute little to CaII and FeII emission. Another paradox of this case would be that SiIV λ 1397 and CIV λ 1549 require different T to account for their intensity ratio. Reverberation mapping of Seyfert nuclei indicates however that the two lines are most close in response times (Korista et al. 1995; Wanders et al. 1997), which is thus inconsistent with a different temperature of the emission line gas.

If the only and dominant source of ionization was mechanical deposition of energy due to shocks and/or friction (shear), our analysis based on photoionization would not be valid. Clearly, an *ad hoc* solution can be found invoking a range of temperatures. However, considering the low EW of all lines in the sources of this paper, and the continuity with the other sources in the E1 sequence, we conclude that there is no convincing evidence that shocks are dominating the emission of HIL and intermediate ionization lines. An additional heating source might significantly affect only the low- T PIZ where most FeII is emitted (Collin & Joly 2000).

6.2. Implications

In §5 we estimate the product $n_{\text{H}} \cdot U$ and now we can compute the distance of the BLR (r_{BLR}) from the central continuum source and the black hole mass (M_{BH}). They are key parameters that allow us to better understand gas dynamics in the emitting region as well as quasar phenomenology and evolution. The dependence of U on r_{BLR} was used to derive black hole masses assuming a plausible average value of the product $n_{\text{H}} \cdot U$. We also use $\text{FWHM}(\text{H}\beta_{\text{BC}})$ under the assumption that the BC arises from a virialized medium

(Padovani et al. 1990; Wandel et al. 1999). Eq. 1 can be rewritten as

$$r_{BLR} = \left[\frac{\int_{\nu_0}^{+\infty} \frac{L_\nu}{h\nu} d\nu}{4\pi n_H U c} \right]^{1/2} \quad (2)$$

and also as

$$r_{BLR} = \frac{1}{h^{1/2} c} (n_H U)^{-1/2} \left(\int_0^{\lambda_{Ly}} f_\lambda \lambda d\lambda \right)^{1/2} d_C \quad (3)$$

where d_C is the the total line-of-sight comoving distance (Hogg & Fruchter 1999):

$$d_C = \frac{c}{H_0} \zeta(z, \Omega_M, \Omega_\Lambda) = \frac{c}{H_0} \int_0^z \frac{dz'}{\sqrt{\Omega_M(1+z)^3 + \Omega_\Lambda}}, \quad (4)$$

where we adopt the Hubble constant $H_0 = 70 \text{ km s}^{-1} \text{ Mpc}^{-1}$. The function ζ has been interpolated as a function of redshift:

$$\zeta(z, \Omega_M, \Omega_\Lambda) \approx [1.500 (1 - e^{-\frac{z}{6.107}}) + 0.996 (1 - e^{-\frac{z}{1.266}})]. \quad (5)$$

with $\Omega_M = 0.3$ and $\Omega_\Lambda = 0.7$, given by Sulentic et al. (2006b).

In equation 3, we transformed the integral from units of frequency to wavelength and rewrote the expression for r_{BLR} in terms of the *rest frame* specific flux f_λ that can be easily derived from the observed flux, namely:

$$L_\nu \nu^{-1} d\nu = 4\pi c^{-1} d_L^2 f_\lambda \lambda d\lambda \quad (6)$$

with d_L the luminosity distance that is related to d_C by the formula $d_L = d_C(1+z)$.

Note that

$$\int_0^{\lambda_{Ly}} f_\lambda \lambda d\lambda = f_{\lambda_0} \cdot \tilde{Q}_H, \quad \text{with} \quad \tilde{Q}_H = \int_0^{\lambda_{Ly}} \tilde{s}_\lambda \lambda d\lambda, \quad (7)$$

where $\lambda_0 = 1700\text{\AA}$. \tilde{Q}_H depends on the shape of the ionizing continuum for a given specific flux with the integral carried out from the Lyman limit to the shortest wavelengths. We use \tilde{s}_λ to define the Spectral Energy Distribution (SED) following Mathews & Ferland (1987) and Laor et al. (1997a) conveniently parameterized as a set of broken power-laws. \tilde{Q}_H is $\approx 0.00963 \text{ cm}\text{\AA}$ in the case of the Laor et al. (1997a) continuum and $\approx 0.02181 \text{ cm}\text{\AA}$ for Mathews & Ferland (1987). We use an average value because the two SEDs give a small difference in estimated number of ionizing photons (see below).

Expressing r_{BLR} in units of light-days, and scaling the variables to convenient units, Eq. 3 becomes:

$$r_{BLR} \approx 93 \left[\frac{f_{\lambda_0, -15} \tilde{Q}_{H, 0.01}}{(n_H U)_{10}} \right]^{\frac{1}{2}} \zeta(z, 0.3, 0.7) \text{ light days}. \quad (8)$$

In this equation, $f_{\lambda_0, -15}$ is the specific rest frame flux (measured on the spectra) in units of $10^{-15} \text{ erg s}^{-1} \text{ cm}^{-2} \text{ \AA}^{-1}$, $\tilde{Q}_{H,0.01}$ is normalized to 10^{-2} cm\AA . The product $n_H U$ is normalized to 10^{10} cm^{-3} , $\zeta(z, 0.3, 0.7)$ is derived from equation 5 and r_{BLR} is now expressed in units of light days.

Knowing r_{BLR} we can calculate the M_{BH} assuming virial motions of the gas

$$M_{\text{BH}} = f \frac{\Delta v^2 r_{\text{BLR}}}{G}. \quad (9)$$

or,

$$M_{\text{BH}} = \frac{3}{4G} f_{0.75} (\text{FWHM})^2 r_{\text{BLR}} \quad (10)$$

with the geometry term $f \approx 0.75$, corresponding to $f_{0.75} \approx 1.0$ (Graham et al. 2011). The factor f depends on the details of the geometry, kinematics, and orientation of the BLR and is expected to be of order unity. This factor converts the measured velocity widths into an intrinsic Keplerian velocity (Peterson & Wandel 2000, Onken et al. 2004, Graham et al. 2011).

Resultant r_{BLR} and M_{BH} estimates are reported in Table 3. Errors in this Table are at 2σ confidence level. They are not symmetrical around this value. They were propagated quadratically, following Barlow (2003, 2004). We consider three sources of uncertainty in the r_{BLR} computations:

1. The error in the determination of n_H and U that is described in detail in §5.1. We use the average value for all of the crossing-points in Figure 6 to define a single $n_H \cdot U$ value which is used in equation 3 to compute the r_{BLR} .

2. The error derived from the shape of the ionizing continuum, which is used in the computation of the r_{BLR} . The two SEDs that we assumed as extreme yield a difference in ionizing photons of a factor 0.17 dex. At a 2σ confidence level this corresponds to an uncertainty in the number of ionizing photons of ± 0.057 dex.

3. Errors in the specific fluxes (at 11700\AA Col. 3 of Tab. 2), intrinsic to the spectrophotometry. We also consider the error in the continuum placement (discussed in §3.2.1).

In the determination of M_{BH} we consider two sources of error.

1. The combined error of the three sources of uncertainties on the r_{BLR} computation described above.

2. The error on the determination of the FWHM, that is discussed at the end of the section 3.2.1.

Using our derivations for n_{H} and U we obtain the r_{BLR} and M_{BH} values listed in Table 3. The last two columns give virial black hole masses following our method and using the $M_{\text{BH}} - \text{luminosity}$ correlation from Vestergaard & Peterson (2006) respectively. Notice that Vestergaard & Peterson (2006) used a different value for the geometry term which is $f = 1.4$ (Onken et al. 2004 and Woo et al. 2010), and the implication in the mass computation is that our masses are a factor of two lower. This was taken into account making the correction $\log(f_{\text{ours}}/f_{\text{V\&P}}) = \log(0.75/1.4) = -0.27$. We subtract this quantity to the Vestergaard & Peterson (2006) M_{BH} formula used to compute the masses in column 7 of Table 3.

The intrinsic dispersion in the Vestergaard & Peterson (2006) relation is ± 0.66 dex in black hole mass at a 2σ confidence level. We are not considering here the scatter in the relation $r_{\text{BLR}} - L$ derived by Bentz et al. (2009) which involves sources where r_{BLR} was derived from reverberation mapping. The scatter in the $r_{\text{BLR}} - L$ correlation is ≈ 0.2 dex in r_{BLR} . These r_{BLR} determinations are, in spite of many caveats recently summarized in Marziani & Sulentic (2012), probably the best ones available. Kaspi et al. (2007) were able to derive one point in the $r_{\text{BLR}} - L$ correlation directly from reverberation mapping of a high- z (2.17) object. Additional observations will allow to check whether the Kaspi empirical relationship holds at high redshift. At the moment we cannot rely on the mass derivation of one source only. The UV extrapolation for single-epoch virial-broadening estimates in Vestergaard & Peterson (2006) shows a much larger scatter but is the only relation that provides M_{BH} a suitable comparison with our result. Errors obtained with our method are a factor of ~ 3 smaller than the dispersion in the Vestergaard & Peterson (2006) relation. However, the latter errors are statistical making the comparison not very straightforward. In a forthcoming paper (Negrete et al. 2012 in preparation) we will give the results of a statistical analysis applying our method to a larger number of quasars than reported here (8 at high- z and 14 at low- z , belonging to both populations A and B). Preliminary results are given in Negrete (2011). These are all Type 1 (broader line) quasars.

6.2.1. Caveats

Our estimation of r_{BLR} assumes that the continuum incident on the line-emitting gas is “as observed” by us. Leighly (2004) suggests (for two IZw1-like sources: IRAS 13224-3809 and 1H0707-495) that a high-ionization wind producing the BLUE component (we fit to the HILs: Marziani et al. 2010) intercepts most of the ionizing flux – leaving only a small fraction available for photoionizing the LIL emitting region. The empirical analysis of their UV spectra is similar to ours with separation of an unshifted BC and BLUE components

(Leighly & Moore 2004). While continuum absorption should not strongly influence the determination of n_{H} and U (they are set by line ratios dependent on physical conditions in the gas) the r_{BLR} value will be affected (Eq. 8). Absorption as extreme as hypothesized by Leighly (2004) (a factor 10) would lead to a decrease of r_{BLR} by ≈ 0.5 dex. However, any consideration is highly dependent on the assumed geometry. The configuration envisaged by Leighly (2004) suffers from an immediate observational difficulty. If the LIL emitting regions were being hit by a wind then the LILs should be emitted by gas ablated from a thick structure and with some of the wind momentum transferred to the ablated gas. There is no observational (kinematical) evidence for this: the LILs and intermediate-ionization lines show stable, unshifted (to within a few hundreds km s^{-1}) and symmetric profiles. It is worth noting that the LILs are even unaffected by the presence of a powerful radio jet in radio-loud quasars (Marziani et al. 2003). In summary, current evidence suggests that the LIL emitting region is not strongly affected by quasar outflows.

7. CONCLUSION

Diagnostic line ratios for estimation of density, ionization and metallicity can be found and exploited for NLSy1-like sources at high redshift. Accurate diagnostics require high S/N and moderate dispersion spectra but in principle can be applied to very high z (> 6.5) using data from IR spectrometers. The product ($n_{\text{H}} \cdot U$) yields the possibility of deriving r_{BLR} and M_{BH} for a significant number of sources for comparison with estimates derived from extrapolation of the Kaspi relation. Negrete et al. (2012, in preparation) will present an analysis of the applicability of the photoionization method described here to the general population of quasars starting from the sources with reverberation mapping determinations of r_{BLR} .

It is important to stress however, that the line deblending that allow us to obtain the line fluxes used to compute n_{H} and U , is not a trivial task. There is a wide diversity in the quasar spectra and one must consider previous results that allow us to predict and/or expect the presence and shape of various components in the broad lines (as discussed in §3.1). One also has to take into account expectations on certain line ratios (e.g. the extreme Pop. A sources show the lowest $\text{CIII}] \lambda 1909 / \text{SiIII}] \lambda 1892$ ratio among all quasars in the E1 sequence, see §3.2.2).

The results of this study are preliminary in many ways. Several issues remain open. 1) Is there a “universal” $n_{\text{H}} \cdot U$ product that can be used for all AGN? The consistency among our results, the ones reviewed in §5.2 and the $r_{\text{BLR}}-L$ relation, suggest that this might be the case, at least to a first approximation and especially for Population A sources. 2) A

grid of simulations could be refined considering more intermediate metallicity cases. 3) Application of this method has been carried out without considerations about the geometry and kinematics of the BLR. A more refined treatment should consider likely scenarios and investigate their influence on derived physical parameters. 4) Considerations of geometry and kinematics could lead to a physical model accounting for non-thermal heating and production of FeII emission in a context more appropriate than that of pure photoionization.

As a final remark, we stress that values of M_{BH} derived from photoionization considerations, even assuming an average $(n_{\text{H}} \cdot U)$ are probably more accurate than the ones derived from the mass- L relation. The main reason is that we are using each individual quasar luminosity (and not a correlation with large scatter) and the properties of a region that remains similar to itself over a wide range of luminosity.

D.Dultzin acknowledges support from grant IN111610 PAPIIT UNAM. Funding for the SDSS and SDSS-II has been provided by the Alfred P. Sloan Foundation, the Participating Institutions, the National Science Foundation, the U.S. Department of Energy, the National Aeronautics and Space Administration, the Japanese Monbukagakusho, the Max Planck Society, and the Higher Education Funding Council for England. The SDSS Web Site is <http://www.sdss.org>. The SDSS is managed by the Astrophysical Research Consortium for the Participating Institutions listed at the <http://www.sdss.org>.

REFERENCES

- Bachev, R., Marziani, P., Sulentic, J. W., Zamanov, R., Calvani, M., & Dultzin-Hacyan, D. 2004, *ApJ*, 617, 171
- Baldwin, J., Ferland, G., Korista, K., & Verner, D. 1995, *ApJL*, 455, L119+
- Baldwin, J. A., Ferland, G. J., Korista, K. T., Hamann, F., & LaCluyzé, A. 2004, *ApJ*, 615, 610
- Baldwin, J. A., et al. 1996, *ApJ*, 461, 664
- Barlow, R. 2003, in *Statistical Problems in Particle Physics, Astrophysics, and Cosmology*, ed. L. Lyons, R. Mount, & R. Reitmeyer, 250–+
- Barlow, R. 2004, *ArXiv Physics e-prints*, arXiv:physics/0406120
- Bentz, M. C., Peterson, B. M., Pogge, R. W., & Vestergaard, M. 2009, *ApJL*, 694, L166

- Bian, W.-H., Huang, K., Hu, C., Zhang, L., Yuan, Q.-R., Huang, K.-L., & Wang, J.-M. 2010, *ApJ*, 718, 460
- Boroson, T. A., & Green, R. F. 1992, *ApJS*, 80, 109
- Callegari, F., & Trigueiros, A. G. 1998, *ApJS*, 119, 181
- Clavel, J., et al. 1991, *ApJ*, 366, 64
- Collin, S., & Joly, M. 2000, *NAR*, 44, 531
- Davidson, K., & Netzer, H. 1979, *Reviews of Modern Physics*, 51, 715
- Dhanda, N., Baldwin, J. A., Bentz, M. C., & Osmer, P. S. 2007, *ApJ*, 658, 804
- Dultzin, D., Martinez, M. L., Marziani, P., Sulentic, J. W., & Negrete, A. 2011, in *Proceedings of the conference "Narrow-Line Seyfert 1 Galaxies and their place in the Universe"*. Ed. L. Foschini et al. Published online at <http://pos.sissa.it/cgi-bin/reader/conf.cgi?confid=126>, id.12
- Dumont, A. M., & Mathez, G. 1981, *A&A*, 102, 1
- Ferland, G. J., Baldwin, J. A., Korista, K. T., Hamann, F., Carswell, R. F., Phillips, M., Wilkes, B., & Williams, R. E. 1996, *ApJ*, 461, 683
- Ferland, G. J., Korista, K. T., Verner, D. A., Ferguson, J. W., Kingdon, J. B., & Verner, E. M. 1998, *PASP*, 110, 761
- Francis, P. J., Hewett, P. C., Foltz, C. B., Chaffee, F. H., Weymann, R. J., & Morris, S. L. 1991, *ApJ*, 373, 465
- Graham, A. W., Onken, C. A., Athanassoula, E., & Combes, F. 2011, *MNRAS*, 412, 2211
- Hartig, G. F., & Baldwin, J. A. 1986, *ApJ*, 302, 64
- Hogg, D. W., & Fruchter, A. S. 1999, *ApJ*, 520, 54
- Johansson, S., Zethson, T., Hartman, H., Ekberg, J. O., Ishibashi, K., Davidson, K., & Gull, T. 2000, *A&Ap*, 361, 977
- Joly, M. 1987, *A&A*, 184, 33
- Joly, M., Véron-Cetty, M., & Véron, P. 2008, in *Revista Mexicana de Astronomia y Astrofisica Conference Series*, Vol. 32, *Revista Mexicana de Astronomia y Astrofisica Conference Series*, 59–61

- Juarez, Y., Maiolino, R., Mujica, R., Pedani, M., Marinoni, S., Nagao, T., Marconi, A., & Oliva, E. 2009, *A&Ap*, 494, L25
- Kaspi, S., Brandt, W. N., Maoz, D., Netzer, H., Schneider, D. P., & Shemmer, O. 2007, *ApJ*, 659, 997
- Korista, K., Baldwin, J., Ferland, G., & Verner, D. 1997, *ApJS*, 108, 401
- Korista, K. T. 1992, *ApJS*, 79, 285
- Korista, K. T., et al. 1995, *ApJS*, 97, 285
- Kriss, G. 1994, *Astronomical Data Analysis Software and Systems III*, A.S.P. Conference Series, 61, 437
- Kuehn, C. A., Baldwin, J. A., Peterson, B. M., & Korista, K. T. 2008, *ApJ*, 673, 69
- Kuraszkiewicz, J. K., Green, P. J., Crenshaw, D. M., Dunn, J., Forster, K., Vestergaard, M., & Aldcroft, T. L. 2004, *ApJS*, 150, 165
- Laor, A., Fiore, F., Elvis, M., Wilkes, B. J., & McDowell, J. C. 1997a, *ApJ*, 477, 93
- Laor, A., Jannuzi, B. T., Green, R. F., & Boroson, T. A. 1997b, *ApJ*, 489, 656
- Leighly, K. M. 2004, *ApJ*, 611, 125
- Leighly, K. M., & Moore, J. R. 2004, *ApJ*, 611, 107
- Leitherer, C., et al. 1999, *ApJS*, 123, 3
- Lipari, S., Terlevich, R., & Macchetto, F. 1993, *ApJ*, 406, 451
- Maiolino, R., et al. 2010, *A&A*, 517, A47+
- Marziani, P., Calvani, M., & Sulentic, J. W. 1992, *ApJ*, 393, 658
- Marziani, P., & Sulentic, J. W. 2012, *New A Rev.*, 56, 49
- Marziani, P., Sulentic, J. W., Negrete, C. A., Dultzin, D., Zamfir, S., & Bachev, R. 2010, *MNRAS*, 409, 1033
- Marziani, P., Sulentic, J. W., Stirpe, G. M., Zamfir, S., & Calvani, M. 2009, *A&Ap*, 495, 83
- Marziani, P., Zamanov, R. K., Sulentic, J. W., & Calvani, M. 2003, *MNRAS*, 345, 1133
- Mathews, W. G., & Ferland, G. J. 1987, *ApJ*, 323, 456

- Matsuoka, Y., Kawara, K., & Oyabu, S. 2008, *ApJ*, 673, 62
- Metzroth, K. G., Onken, C. A., & Peterson, B. M. 2006, *ApJ*, 647, 901
- Negrete, C. A. 2011, PhD thesis, UNAM, Mexico, (2011)
- Netzer, H., & Marziani, P. 2010, *ApJ*, 724, 318
- Netzer, H., & Trakhtenbrot, B. 2007, *ApJ*, 654, 754
- Nussbaumer, H., & Storey, P. J. 1982, *A&A*, 115, 205
- Onken, C. A., Ferrarese, L., Merritt, D., Peterson, B. M., Pogge, R. W., Vestergaard, M., & Wandel, A. 2004, *ApJ*, 615, 645
- Onken, C. A., & Peterson, B. M. 2002, *ApJ*, 572, 746
- Osterbrock, D. E., & Ferland, G. J. 2006, *Astrophysics of gaseous nebulae and active galactic nuclei* (University Science Books)
- Padovani, P., Burg, R., & Edelson, R. A. 1990, *ApJ*, 353, 438
- Padovani, P., & Rafanelli, P. 1988, *A&A*, 205, 53
- Peterson, B. M. 2011, in Proceedings of the conference "Narrow-Line Seyfert 1 Galaxies and their place in the Universe". April 4-6, 2011. Milano, Italy. L. Foschini et al. (Editors), id.32, Proceedings of Science
- Peterson, B. M., & Wandel, A. 2000, *ApJ*, 540, L13
- Peterson, B. M., et al. 2002, *ApJ*, 581, 197
- . 2004, *ApJ*, 613, 682
- Rees, M. J., Netzer, H., & Ferland, G. J. 1989, *ApJ*, 347, 640
- Shields, G. A., Ludwig, R. R., & Salviander, S. 2010, *ApJ*, 721, 1835
- Sigut, T. A. A., & Pradhan, A. K. 2003, *ApJS*, 145, 15
- Sigut, T. A. A., Pradhan, A. K., & Nahar, S. N. 2004, *ApJ*, 611, 81
- Simon, L. E., & Hamann, F. 2010, *MNRAS*, 407, 1826
- Sulentic, J. W., Bachev, R., Marziani, P., Negrete, C. A., & Dultzin, D. 2007, *ApJ*, 666, 757

- Sulentic, J. W., Dultzin-Hacyan, D., Marziani, P., Bongardo, C., Braitto, V., Calvani, M., & Zamanov, R. 2006a, *Revista Mexicana de Astronomia y Astrofisica*, 42, 23
- Sulentic, J. W., Marziani, P., & Dultzin-Hacyan, D. 2000, *ARA&A*, 38, 521
- Sulentic, J. W., Marziani, P., Zamanov, R., Bachev, R., Calvani, M., & Dultzin-Hacyan, D. 2002, *ApJL*, 566, L71
- Sulentic, J. W., Repetto, P., Stirpe, G. M., Marziani, P., Dultzin-Hacyan, D., & Calvani, M. 2006b, *A&Ap*, 456, 929
- Sulentic, J. W., Stirpe, G. M., Marziani, P., Zamanov, R., Calvani, M., & Braitto, V. 2004, *A&Ap*, 423, 121
- Vanden Berk, D. E., et al. 2001, *AJ*, 122, 549
- Vestergaard, M., & Peterson, B. M. 2005, *ApJ*, 625, 688
- . 2006, *ApJ*, 641, 689
- Vestergaard, M., & Wilkes, B. J. 2001, *ApJS*, 134, 1
- Wandel, A., Peterson, B. M., & Malkan, M. A. 1999, *ApJ*, 526, 579
- Wanders, I., et al. 1997, *ApJS*, 113, 69
- Wang, H., Wang, T., Zhou, H., Liu, B., Wang, J., Yuan, W., & Dong, X. 2011, *ArXiv e-prints*
- Wills, D., & Netzer, H. 1979, *ApJ*, 233, 1
- Woo, J.-H., et al. 2010, *ApJ*, 716, 269
- Woosley, S. E., & Weaver, T. A. 1995, *ApJS*, 101, 181
- Zamfir, S., Sulentic, J. W., Marziani, P., & Dultzin, D. 2010, *MNRAS*, 403, 1759

Table 1. Line Components in the $\lambda 1900$ blend

Ion	λ Å	X eV	$E_l - E_u$ eV	Transition	A_{ki} s ⁻¹	n_c cm ⁻³	Note
(1)	(2)	(3)	(4)	(5)	(6)	(7)	(8)
Si II	1808.00	8.15	0.000 - 6.857	$^2D_{3/2}^o \rightarrow ^2P_{1/2}$	$2.54 \cdot 10^6$...	1
Si II	1816.92	8.15	0.036 - 6.859	$^2D_{5/2}^o \rightarrow ^2P_{3/2}$	$2.65 \cdot 10^6$...	1
Al III	1854.716	18.83	0.000 - 6.685	$^2P_{3/2}^o \rightarrow ^2S_{1/2}$	$5.40 \cdot 10^8$...	1
Al III	1862.790	18.83	0.000 - 6.656	$^2P_{1/2}^o \rightarrow ^2S_{1/2}$	$5.33 \cdot 10^8$...	1
[Si III]	1882.7	16.34	0.000 - 6.585	$^3P_2^o \rightarrow ^1S_0$	0.012	$6.4 \cdot 10^4$	1 2 3
Si III]	1892.03	16.34	0.000 - 6.553	$^3P_1^o \rightarrow ^1S_0$	16700	$2.1 \cdot 10^{11}$	1 4 5
[C III]	1906.7	24.38	0.000 - 6.502	$^3P_2^o \rightarrow ^1S_0$	0.0052	$7.7 \cdot 10^4$	1 2 6
C III]	1908.734	24.38	0.000 - 6.495	$^3P_1^o \rightarrow ^1S_0$	114	$1.4 \cdot 10^{10}$	1 2 4 5
Fe III	1914.066	16.18	3.727 - 10.200	$z^7P_3^o \rightarrow a^7S_3$	$6.6 \cdot 10^8$...	7

Note. — All wavelengths are in vacuum.

(1) Ralchenko, Yu., Kramida, A.E., Reader, J., and NIST ASD Team (2008). NIST Atomic Spectra Database (version 3.1.5). Available at: <http://physics.nist.gov/asd3>.

(2) Feibelman & Aller (1987).

(3) n_c computed following Shaw & Dufour (1995).

(4) Morton (1991).

(5) Feldman (1992).

(6) Zheng (1988).

(7) Wavelength and A_{ki} from Ekberg (1993), energy levels from Edlén and Swings (1942).

Table 2. Measured quantities

Object	z	$f_\lambda(1700 \text{ \AA})^a$	SiIV $\lambda 1397^b$	CIV $\lambda 1549^b$	SiII $\lambda 1814^b$	AlIII $\lambda 1860^b$	SiIII] $\lambda 1892^b$	CIII] $\lambda 1909^b$	FWHM ^c
(1)	(2)	(3)	(4)	(5)	(6)	(7)	(8)	(9)	(10)
I Zw 1	0.0605	$2.7^{+0.3}_{-0.2}$	$27.4^{+6.0}_{-3.5}$	$28.4^{+5.4}_{-4.6}$	$5.4^{+3.7}_{-3.0}$	$18.9^{+2.9}_{-3.3}$	$31.1^{+5.5}_{-5.7}$	$19.0^{+2.5}_{-3.5}$	1050 ± 200
SDSS J1201+0116	3.2332	1.6 ± 0.2	$14.3^{+2.6}_{-3.2}$	$15.5^{+4.3}_{-2.5}$	$5.5^{+3.0}_{-3.2}$	$11.9^{+2.4}_{-2.3}$	$12.7^{+2.4}_{-1.8}$	$2.6^{+3.2}_{-1.8}$	4000 ± 400

^aRest-frame specific continuum flux at 1700 Å in units of $10^{-14} \text{ erg s}^{-1} \text{ cm}^{-2} \text{ \AA}^{-1}$.

^bRest-frame line flux of intermediate ionization line BC and of the CIV $\lambda 1549$ BC in units of $10^{-14} \text{ erg s}^{-1} \text{ cm}^{-2}$.

^cRest frame FWHM of intermediate ionization line BC and of the CIV $\lambda 1549$ BC in units of km s^{-1} .

Table 3. Derived quantities

Object (1)	$\log n_{\text{H}}^{\text{a}}$ (2)	$\log U$ (3)	$\log(n_{\text{H}}U)$ (4)	$\log r_{\text{BLR}}^{\text{b}}$ (5)	$\log M_{\text{BH}}^{\text{c}}$ (6)	$\log M_{\text{BH}}(\text{VP06})^{\text{d}}$ (7)
I Zw 1	$12.00^{+0.32}_{-0.23}$	$-2.65^{+0.21}_{-0.11}$	$9.35^{+0.33}_{-0.23}$	$17.30^{+0.17}_{-0.12}$	$7.30^{+0.23}_{-0.19}$	6.70
SDSS J1201+0116	$12.63^{+0.28}_{-0.24}$	$-2.79^{+0.12}_{-0.06}$	$9.84^{+0.28}_{-0.23}$	$18.31^{+0.14}_{-0.12}$	$9.39^{+0.17}_{-0.15}$	9.29

^a n_{H} in units of cm^{-3} .

^b r_{BLR} in units of cm.

^c M_{BH} in units of M_{\odot} computed with the FWHM values of Table 2.

^d $M_{\text{BH}} \pm 0.66$ dex at a 2σ confidence level, in units of M_{\odot} computed following Vestergaard & Peterson (2006), and input parameters reported in note (b). See text for details.

Table 4. Results from previous studies

Reference	$\log n_{\text{H}}$	$\log U$	$\log(n_{\text{H}}U)$	line
Matsuoka et al. (2008)	12.	-2.5 – -2.0	9.5 – 10	Ca IR Triplet
Sigut & Pradhan (2003)	11.6	-2.0	9.6	their model B for FeII
Padovani & Rafanelli (1988)	–	–	9.8 ± 0.3	H β
Baldwin et al. (1996)	12.7	-2.5	~ 10.2	$\lambda 1900$ blend

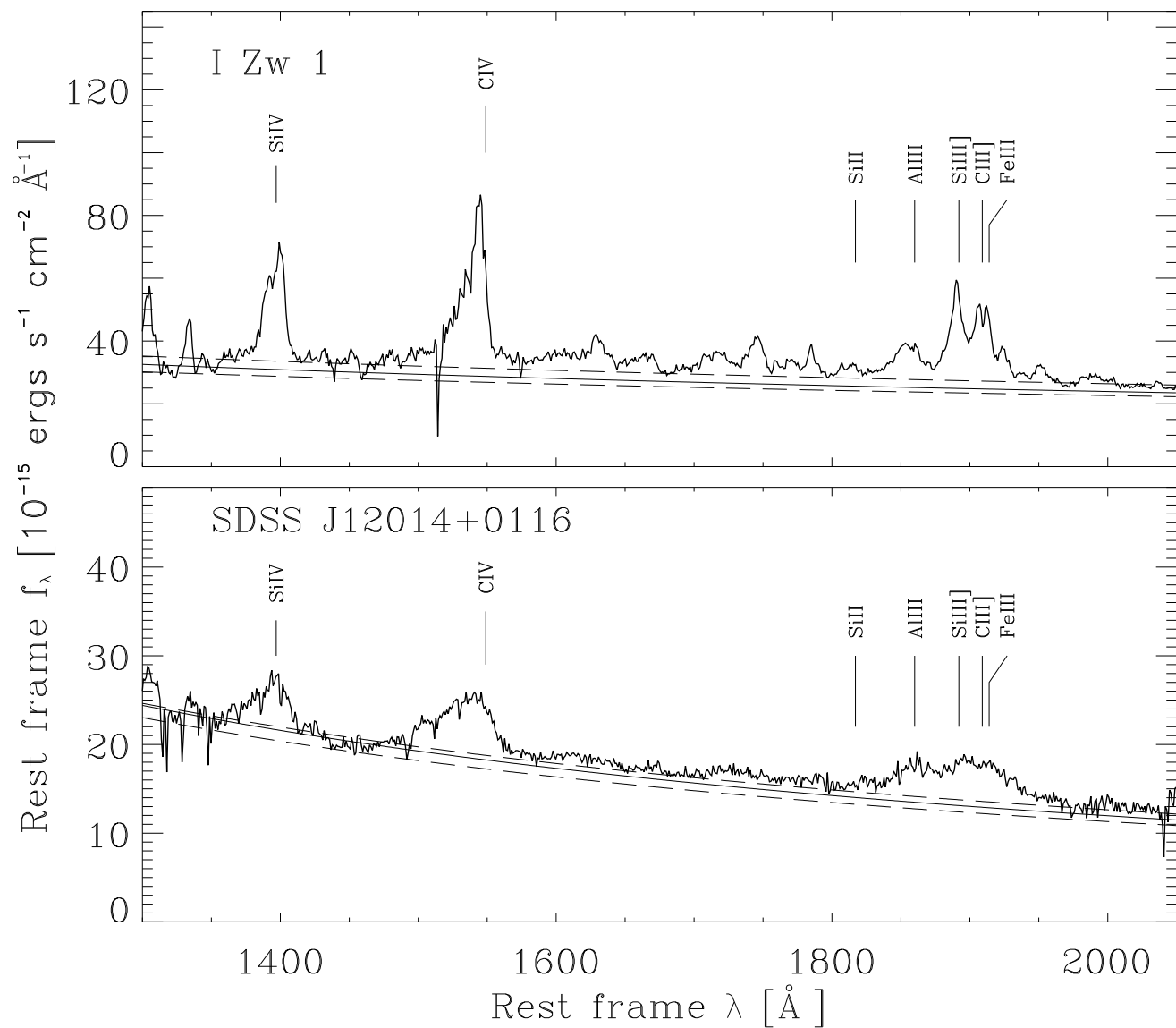


Fig. 1.— Spectra of the two quasars in rest frame wavelength. Upper panel: I Zw 1; lower panel: SDSS J1201+0116. Abscissa is rest frame in \AA , ordinate is specific flux in the rest frame in units 10^{-13} ergs s^{-1} cm^{-2} \AA^{-1} . For both objects, the solid line shows the adopted continuum. Dashed lines under and above are the extreme cases. The principal emission lines are labeled.

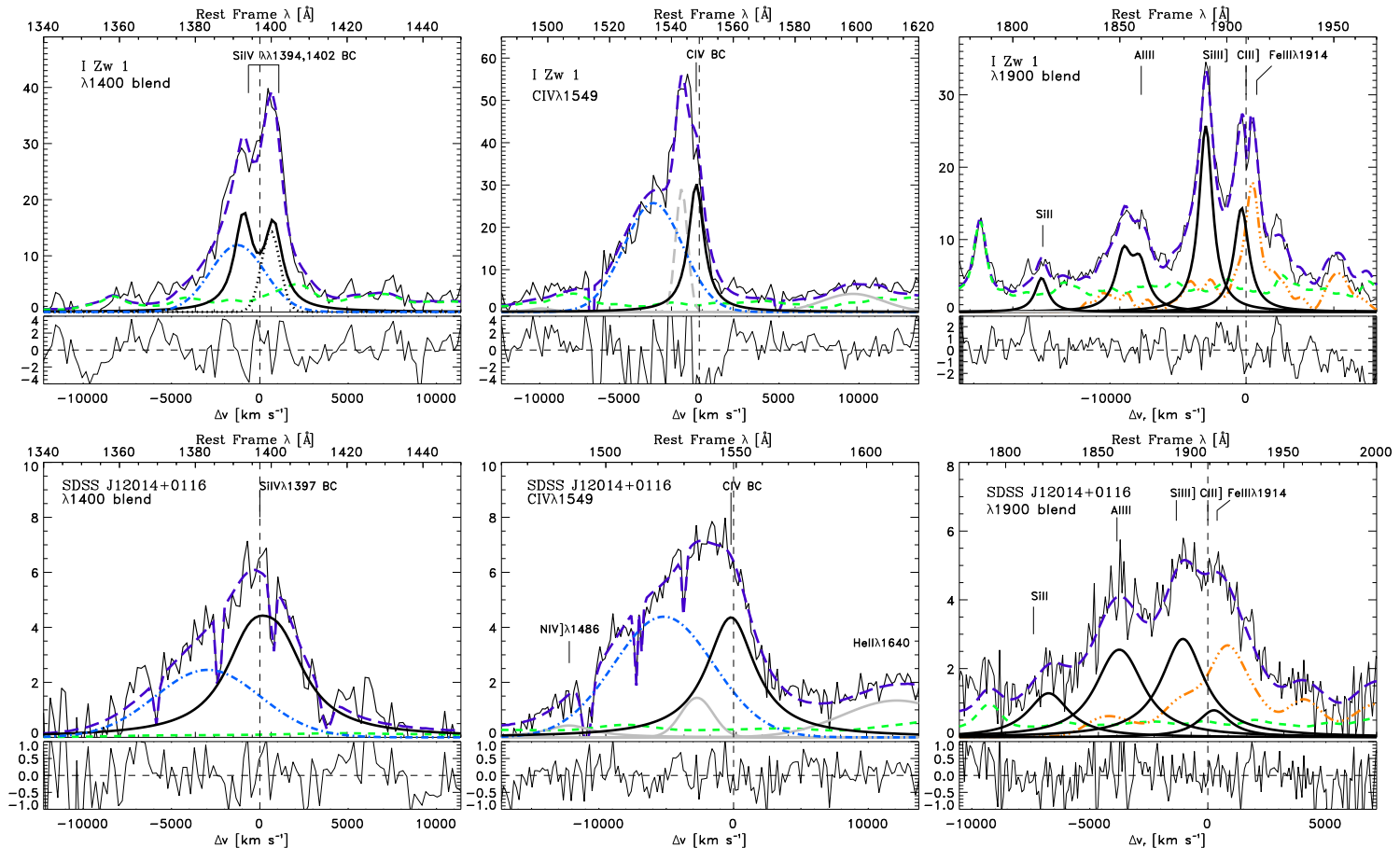


Fig. 2.— We show the fits to SiIV λ 1397 (a doublet, here we show the sum, *left*), CIV λ 1549 (*middle*) and 1900 \AA (*right*) spectral region of I Zw 1 (*top*) and SDSS J12014+0116 (*bottom*). The lower panels show the residuals to the fits. Upper abscissa is rest frame wavelength in \AA , lower abscissa is in velocity units. Vertical dashed line is the rest frame for SiIV λ 1397, CIV λ 1549 and CIII] λ 1909. The vertical scale is rest-frame specific flux in units of $10^{-15}\text{ergs s}^{-1}\text{cm}^{-2}\text{\AA}^{-1}$. The long-dashed purple lines are the fits. Solid black lines are the broad central components. Short-dashed green lines represent the FeII template emission. The dot-dashed blue line in SiIV λ 1397 and in CIV λ 1549 corresponds to the BLUE component. In I Zw 1, the dotted line is the contribution of OIV] λ 1402, and the dashed grey line is the narrow component of CIV λ 1549. For both objects the solid grey lines in CIV λ 1549 represents the contribution of various underlying weaker emission lines. The major constituents of the 1900 \AA blend are AlIII λ 1860 (we show the sum of this doublet), SiIII] λ 1892 and FeIII. The triple-dotted-dashed orange line is the FeIII template plus the FeIII1914 emission line. See text for details.

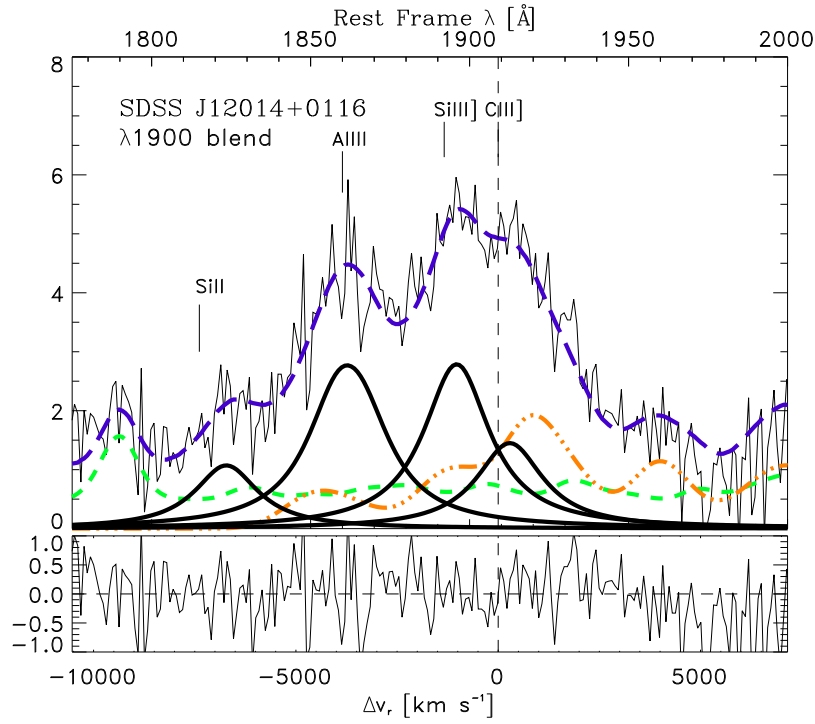


Fig. 3.— Fits to the $\text{H}1900\text{\AA}$ blend of SDSS J12014+0116. In contrast to the lower right panel of Figure 2, here we show the maximum contribution of C III] $\lambda 1909$ line, when the Fe III $\text{H}1914$ emission line is absent. The triple-dotted-dashed orange line is the Fe III template only. Units and symbols are the same as in Fig. 2. See text for details.

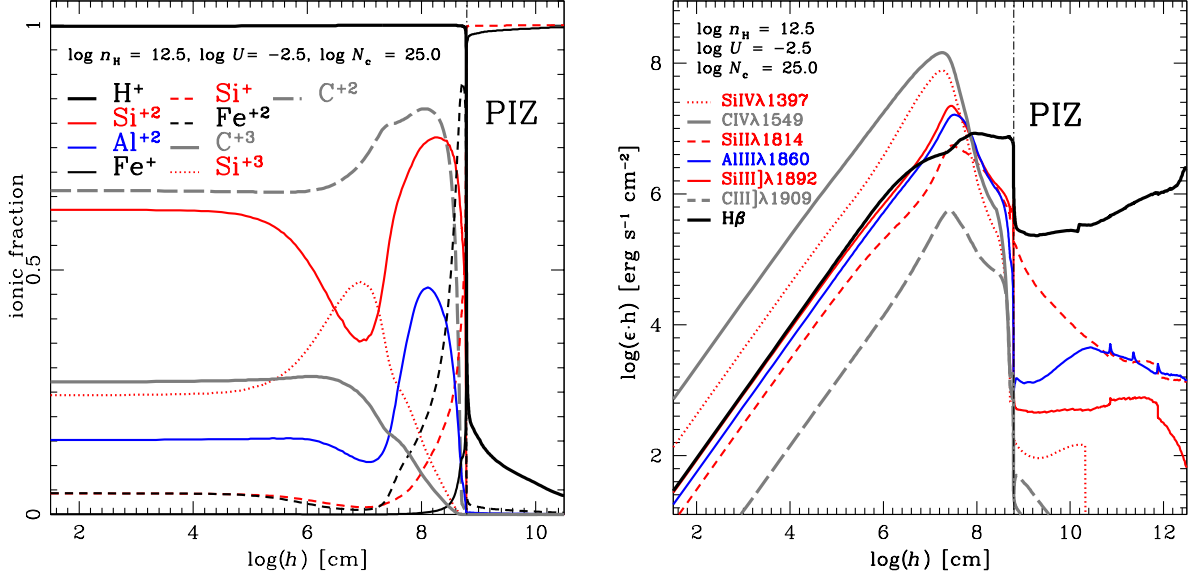


Fig. 4.— We show the result of CLOUDY simulations for the behavior of the emission lines in a gas slab. Left: Ionic Fractions as a function of the logarithm of geometric depth h in a gas slab. Plotted ionic stages (H^+ , thick solid black; Si^{+2} , solid red; Al^{+2} , solid blue; Fe^+ , solid black; Si^+ , dashed red; Fe^{+2} , dashed black; C^{+3} , thick grey; Si^{+3} , dotted red) are the ones relevant to the emission lines considered in this paper. Right: Local line emissivity per unit volume in units of $\text{ergs s}^{-1} \text{cm}^{-3}$ multiplied by depth h in cm as a function of the logarithm of h for $SiIV\lambda 1397$ (red dotted), $CIV\lambda 1549$ (thick grey), $SiII\lambda 1814$ (dashed red), $AlIII\lambda 1860$ (solid blue), $SiIII\lambda 1892$ (solid red), $CIII]\lambda 1909$ (thick dashed grey), $H\beta$ (thick black). The continuum photons enter from left. The partially ionized zone (PIZ) is on the right side of the dot-dashed line. Ionic fraction and emissivity are calculated through a dedicated CLOUDY simulation extending up to $N_c = 10^{25} \text{cm}^{-2}$.

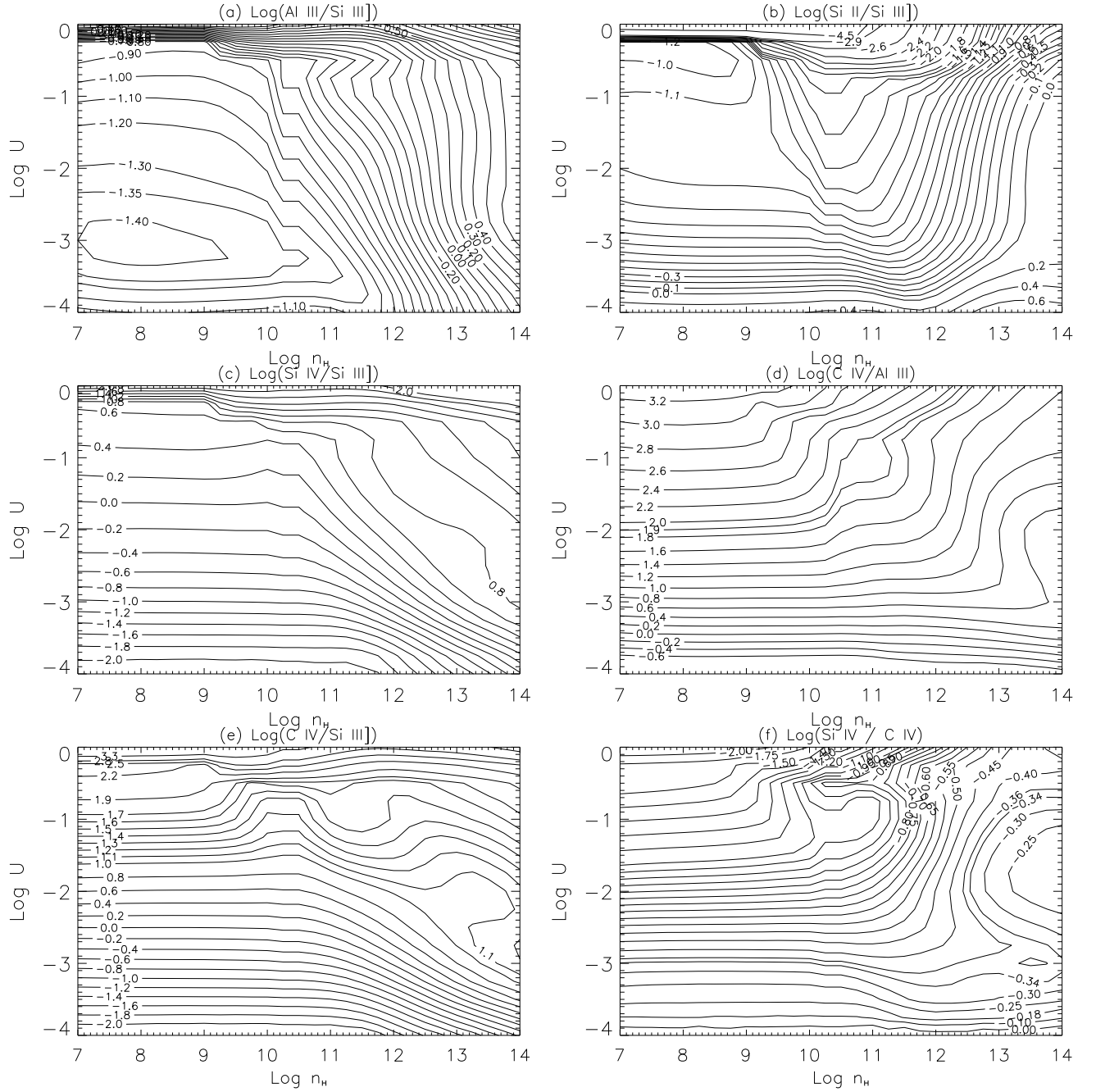


Fig. 5.— Iso-contours of the CLOUDY simulations of the line ratios (a) $\log(\text{AlIII}\lambda 1860/\text{SiII}\lambda 1892)$, (b) $\log(\text{SiII}\lambda 1814/\text{SiII}\lambda 1892)$, (c) $\log(\text{SiIV}\lambda 1397/\text{SiII}\lambda 1892)$, (d) $\log(\text{CIV}\lambda 1549/\text{AlIII}\lambda 1860)$, (e) $\log(\text{CIV}\lambda 1549/\text{SiII}\lambda 1892)$ and (f) $\log(\text{SiIV}\lambda 1397/\text{CIV}\lambda 1549)$. We use a standard value of $N_{\text{c}}=10^{23}$ and solar metallicity. Abscissa is hydrogen density in cm^{-3} , ordinate is the ionization parameter, both in logarithm scale.

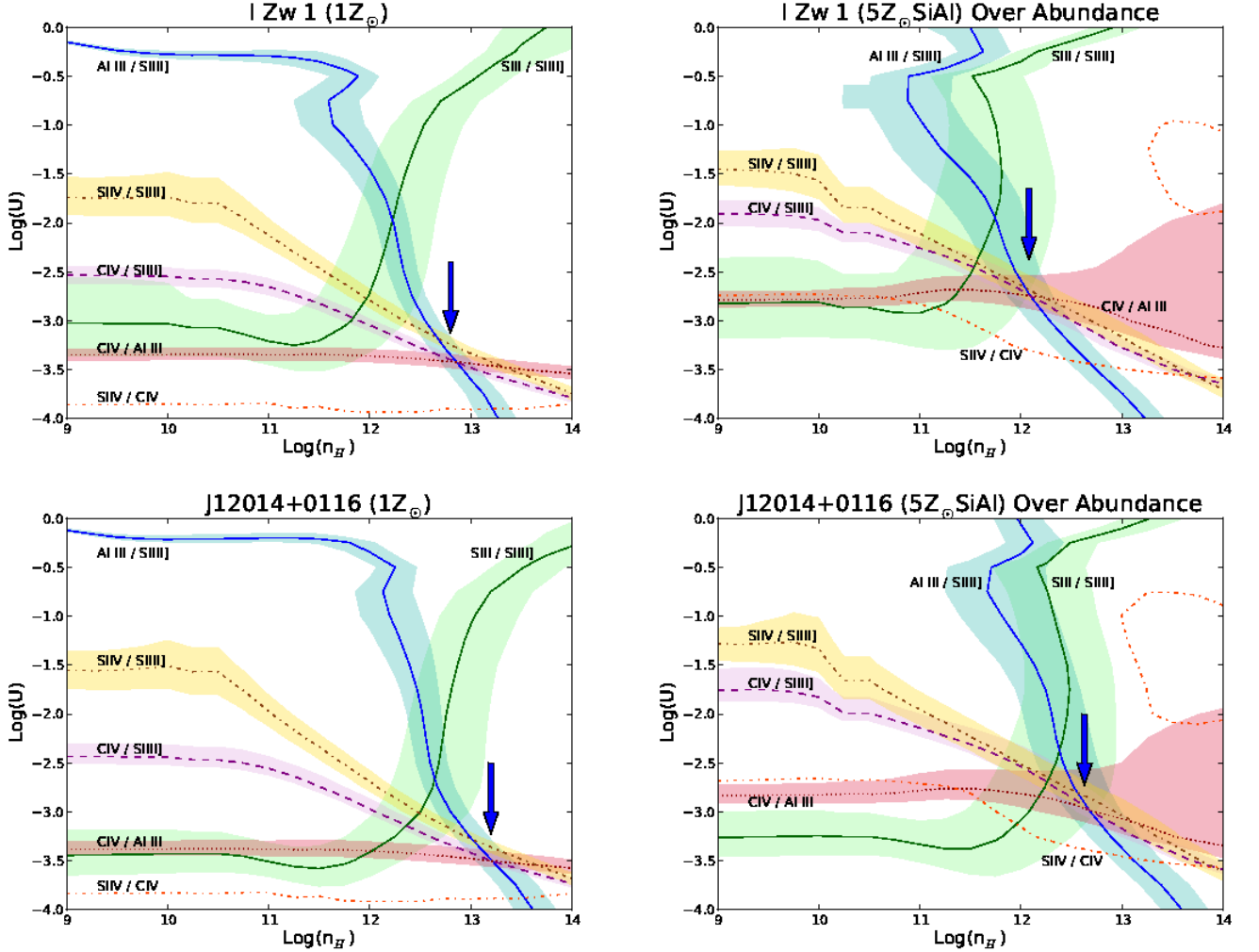


Fig. 6.— Iso-contours for I Zw 1 (top) and SDSS J12014+0116 (bottom). We select the contours of the CLOUDY simulations from Figure 5, which correspond to the measured line ratio from the observed spectra (Table 2). The left panels refer to the case of solar metallicity; the right ones to the case of five times solar plus an overabundance of Si and Al with respect to carbon by a factor 3, described in §4.2 ($5Z_{\odot}\text{SiAl}$). Each arrow points toward the point of convergence that defines the most likely value of U and n_{H} . The bands are the uncertainty bands of the ratios (except for $\text{SiIV}\lambda 1397/\text{CIV}\lambda 1549$). Note that the $\text{SiIV}\lambda 1397/\text{CIV}\lambda 1549$ ratio is not a useful constraint in the $5Z_{\odot}\text{SiAl}$ case, since it varies little in a wide area around the intersection point in the (n_{H}, U) plane.